JOURNAL OF GEOPHYSICAL RESEARCH, VOL. 92, NO. C2, PAGES 1861–1884, FEBRUARY 15, 1987

The Large-Scale Coastal Wind Field Along the West Coast of North America, 1981–1982

GEORGE R. HALLIWELL, JR.,[1] AND J. S. ALLEN

College of Oceanography, Oregon State University, Corvallis

We study the statistical properties of the coastal wind field along the west coast of North America for two summers, 1981 and 1982 (Coastal Ocean Dynamics Experiments 1 and 2, respectively), and the intervening winter using measured winds and geostrophic winds calculated from Fleet Numerical Oceanography Center atmospheric pressure analyses. Summer wind fluctuations are driven primarily by the interaction between two relatively stationary pressure systems, the North Pacific subtropical high and southwest U.S. thermal low, and by their interactions with propagating atmospheric systems to the north. In particular, propagating cyclones and associated fronts are often followed by a northeastward intensification of the high, producing strong upwelling events along the California coast. This summer event sequence occurs more frequently and is displaced farther to the south on average during summer 1981. Winter wind fluctuations are primarily driven by propagating cyclones and anticyclones, and they tend to have larger variance and space scales than in summer. A preference for poleward (equatorward) propagation exists in summer (winter), and the largest time scales are observed in summer 1982. Coastal atmospheric boundary layer processes substantially modify winds within 100–200 km of the coast. Consequently, measured wind fluctuations are strongly polarized in the alongshore direction and have means and rms amplitudes that can vary considerably between nearby stations along the coast. Calculated wind fluctuations are less polarized in the alongshore direction and have alongshore correlation scales about 60% larger than those for measured winds. They represent fluctuations with alongshore wavelengths of $\geqq 900$ km rather well but represent poorly those with smaller wavelengths and those due to coastal atmospheric boundary layer effects.

1. INTRODUCTION

A major goal of the large-scale component of the Coastal Ocean Dynamics Experiment (CODE) is to study the large-scale response (alongshore scales $\gg$ shelf/slope width) of continental shelf currents and coastal sea level to atmospheric forcing along the west coast of North America. The alongshore component of wind stress is an important forcing mechanism for this response, which in simple theories takes the form of forced coastally trapped waves [*Gill and Schumann*, 1974; *Clarke*, 1977]. The large-scale wind fluctuations that effectively drive this current and sea level response [*Halliwell and Allen*, 1987] are primarily caused by synoptic-scale atmospheric pressure systems (cyclones and anticyclones) that have space scales larger than several hundred kilometers and time scales longer than about 2 days. Execution of CODE large-scale component studies therefore requires coastal wind data to be collected along several thousand kilometers of the west coast of North America.

In this paper we study the properties of large-scale coastal wind fluctuations during the two intensive field experiments CODE 1 (summer 1981) and CODE 2 (summer 1982) and during the intervening winter. We focus on properties that are important for driving coastal currents, and we document seasonal variations of these properties. In summer, large-scale wind fluctuations are driven primarily by the variable pressure gradient between two relatively stationary pressure systems: the North Pacific subtropical high, typically located between 20° and 50°N over the eastern North Pacific, and the interior thermal low which is normally centered over the southwestern United States. These wind fluctuations can be substantially modified in the coastal atmospheric boundary layer over the continental shelf and slope [*Beardsley et al.*, this issue; *Mass et al.*, 1986; *Dorman*, 1985, this issue]. In summer a strong temperature inversion caps a surface layer of cool marine air within the domain of the North Pacific subtropical high [*Neiburger et al.*, 1961]. The inversion layer slopes downward toward the coast and intersects the coastal mountains throughout most of the CODE large-scale domain. This blocks the across-shore component of low-level winds, inhibiting geostrophic adjustment to the near-surface atmospheric pressure field when isobars are not parallel to the coast. Coastal winds can therefore have a substantial ageostrophic component, and coastally trapped baroclinic pressure and wind fluctuations may exist. In winter, coastal wind fluctuations are driven primarily by propagating pressure systems (cyclones and anticyclones), and the existence of the marine inversion layer is often interrupted by the strong winds generated by these systems [*Neiburger et al.*, 1961; *Beardsley et al.*, this issue]. Consequently, seasonal cycles in the properties of both synoptic-scale atmospheric pressure systems and the coastal marine boundary layer contribute to the observed seasonal changes in coastal wind properties.

We analyze two representations of the coastal wind field. The first is a set of wind measurements from stations located at or near the coast and from buoys moored on the adjacent continental shelf. The second is a set of geostrophic winds calculated from the 6-hourly surface atmospheric pressure analyses of the Fleet Numerical Oceanography Center (FNOC) [*Bakun*, 1975], which are hereinafter referred to as calculated winds. A simple boundary layer correction is performed on these winds, consisting of a 30% reduction in speed and a 15° anticlockwise rotation. The data from which the pressure analyses are constructed are sampled at both ships and fixed land and buoy stations. This input data consists of

[1]Now at Graduate School of Oceanography, University of Rhode Island, Narragansett.

Paper number 6C0500.
0148-0227/87/006C-0500$05.00

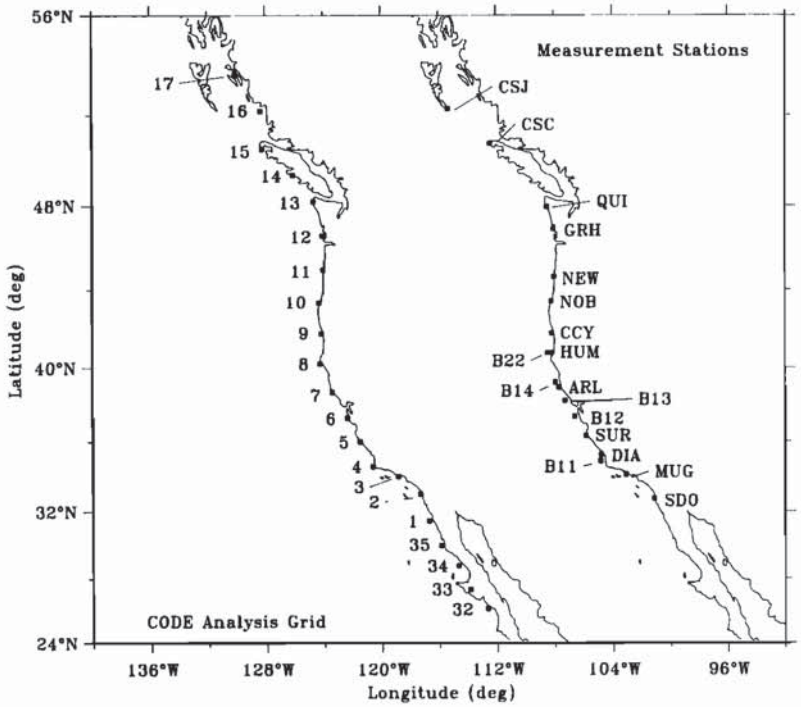

Fig. 1. The coastal points of the CODE analysis grid (left coastline) and the wind measurement stations used in this study (right coastline). The longitude axis is correct for the left coastline. Information on the stations and grid points is summarized in Tables 1 and 2.

both surface pressure and equivalent pressure gradient calculated from surface winds assuming geostrophic balance. These data are blended with an initial best guess surface pressure field determined from previous analyses to generate the new pressure analysis. This procedure is described in detail by *Holl and Mendenhall* [1971].

Measured winds should ideally be used to calculate the wind stress forcing function for shelf currents, but they have numerous problems, including topographic influence, data gaps, irregular sampling times, and sometimes human subjectivity in reading fluctuating anemometer analog displays. The problems with calculated winds include a spatial sampling resolution that restricts their use to studies of large-scale variability only, decreasing accuracy in the geostrophic approximation with decreasing latitude, variable spatial and temporal coverage with ship pressure and wind observations, and an inaccurate boundary layer correction in coastal regions (section 2.2; see also *Halliwell and Allen* [1984]). We therefore analyze both wind sets to characterize the large-scale, low-frequency properties of the coastal wind field. We also compare both wind sets with each other to assess the differences between their properties. The evaluation of the two wind sets as atmospheric forcing functions is presented in our studies of the coastal sea level response to wind stress [*Halliwell and Allen*, 1984, 1987].

We first describe the data sets and discuss the boundary layer correction for calculated winds (section 2). We present the basic statistical properties of the coastal wind field, emphasizing interannual and seasonal similarities and differences (section 3). We document frequency domain and wave number–frequency domain properties of wind fluctuations using spectrum analysis (section 4). We relate these statistical properties to those of wind events and synoptic-scale atmospheric systems by studying alongshore time contour plots of calculated and measured winds and surface atmospheric pressure charts (section 5). We focus primarily on the properties of the alongshore component of the wind, since this is theoretically the most important component for driving large-scale coastally trapped waves and since *Halliwell and Allen* [1984] noted that the component of measured vector wind stress within the CODE large-scale domain that is most correlated with sea level is oriented approximately alongshore. Analyses of the vector and across-shore winds are also presented wherever they illustrate important properties of the wind field.

TABLE 1. Coastal Points of the CODE Large-Scale Analysis Grid

Point Number	North Latitude	West Longitude	y, km	Coast Orientation
17	54°09′	130°20′	1800	120
16	52°10′	128°19′	1620	115
15	50°32′	127°13′	1440	100
14	49°23′	126°06′	1260	128
13	48°11′	124°42′	1080	120
12	46°36′	124°05′	900	95
11	44°58′	124°03′	720	85
10	43°21′	124°20′	540	73
09	41°46′	124°12′	360	103
08	40°12′	124°18′	180	130
07	38°42′	123°27′	0	133
06	37°18′	122°24′	−180	102
05	35°59′	121°31′	−360	128
04	34°35′	120°39′	−540	90
03	34°01′	118°53′	−720	150
02	33°00′	117°21′	−900	110
01	31°27′	116°44′	−1080	110
35	30°00′	115°54′	−1260	115
34	28°47′	114°41′	−1440	130
33	27°20′	113°52′	−1620	130
32	26°07′	112°40′	−1800	130

Coast orientation is measured in degrees anticlockwise from due east. Data from odd points between 1 and 17 and from 32 and 34 are used in Figures 3 and 5.

2. THE DATA SET

2.1. *Data and Data Processing*

The CODE large-scale analysis domain extends from northern Baja California (26°N) to the Alaska border (54°N) to resolve the large alongshore scales of the wind field and the coastally trapped wave response. The coastal alongshore coordinate y is zero at the location of the CODE central line and positive poleward of that location. We use calculated winds that are interpolated to the locations of the CODE analysis grid (Figure 1, Table 1), with grid point 7 located at $y = 0$ km. The alongshore separation of the grid points is 180 km, and the grid spans 3600 km of coastline. The CODE experimental site [*Winant et al.*, this issue] is located approximately within the interval $-50 < y < 50$ km. Alongshore separations are estimated from coastal charts by measuring the distance following a smoothed shoreline, i.e., by ignoring deviations due to small bays and headlands that span less than about 20 km of coast.

We study three time intervals of four months duration: (1) 1200 UT April 3 to 1800 UT July 31, 1981 (119.5 days); (2) 0000 UT December 1, 1981, to 1800 UT March 31, 1982 (121 days); and (3) 0000 UT May 1 to 1800 UT August 31, 1982 (123 days). The first 4-month interval was shortened by 2.5 days at the beginning because of missing data. We refer to these intervals as summer 1981, winter 1981–1982, and summer 1982. The two summer seasons are chosen both to coincide with the intensive instrument deployments of the CODE 1 and CODE 2 experiments [*Winant et al.*, this issue] and to span the period of strongest coastal upwelling. Therefore the seasonal differences in wind field properties that we document in this study represent those between the periods of strongest upwelling and strongest downwelling over the continental shelf. The winter season is essentially centered about the period of strongest winter storminess in the atmosphere, but the two summer seasons are not centered on the summer minimum in storminess. Consequently, we do not document the full seasonal range of properties of the coastal wind field in this study.

Measured winds are available at over 70 locations along the coast during the CODE experiment. These measurements are obtained from numerous sources, with information about them, including discussions of the editorial procedures used and the basic statistical properties of all of the data, documented by *Halliwell and Allen* [1983, 1985] and *Halliwell et al.* [1986]. The basic editorial steps performed on both measured and calculated winds include conversion of winds to north-south and east-west (u and v) components, conversion to common units of meters per second, and deletion of obviously bad data points. All gaps less than 12 hours in length are filled by linear interpolation. The resulting time series are low-pass filtered (half-amplitude period = 40 hr) and have a sampling rate of 6 hours. Linear trends are removed from the time series prior to performing all statistical analyses.

We select the subset of wind measurement stations analyzed in this study by choosing the best possible stations that have alongshore separations as close as possible to the separation between CODE grid points ($\Delta y = 180$ km). National Data Buoy Center (NDBC) offshore buoy winds are used wherever possible. For the remaining stations the best are identified by studying the basic wind statistics to determine if local effects, such as topography, influence the wind, then by comparing measured and calculated winds under the assumption that the measured winds best correlated with calculated winds are least influenced by local effects. The alongshore spacing of the selected stations is reasonably good along the U.S. coast, but is too large along the British Columbia coast because of an insufficient number of good stations (Figure 1 and Table 2). Owing to the presence of long data gaps, the identical set of stations could not be used for all three seasons. Several shorter gaps in the selected stations have been filled by linear regression from nearby stations not used in the analyses: (1) GRH, 0600 UT August 22 to 1800 UT August 31, 1982, filled using HOQ; (2) CCY, 0000 UT May 1 to 0600 UT May 5, 1982, filled using PSG; (3) B22, 0000 UT December 1, 1981, to 0600 UT January 21, 1982, filled using ACA; and (4) B12, 0600 UT January 24 to 1800 UT March 31 1982, filled using PIG. The additional stations used in these interpolations are also listed in Table 1. For the integral correlation space and time scale analysis in section 3.6 and the wave number–frequency spectrum analyses in Section 4.2, measured wind components are interpolated to the CODE large-scale analysis grid by a cubic spline interpolation in the alongshore direction at each sampling time.

2.2. *The Rotation Correction for Calculated Winds*

Several studies have determined that the 15° anticlockwise rotation performed as part of the original boundary layer correction is not sufficient. These include the study of *Halliwell and Allen* [1984] for the west coast of North America, plus the wind analyses of *Thomson* [1983] for the British Columbia coast and *Hsueh and Romea* [1983] for the East China Sea. (Hsueh and Romea calculated geostrophic winds using pressure from surface meteorological charts.) Because of this, *Halliwell and Allen* [1984] rotated calculated winds to align their fluctuations with those of measured winds prior to calculating the alongshore component of the calculated winds. Since we have assembled a much-improved measured wind set for the CODE study that also includes winter measurements, we recalculate the rotation corrections here and determine if they have seasonal variability. This correction was performed prior to computing the alongshore and across-shore components of the calculated winds used in these analyses. However, all analyses of calculated vector wind components u and v, which include basic statistics, principal axes, complex correlations, and rotary autospectra and cross-spectra, are performed using the original, uncorrected winds, since the effects of the misalignment between calculated and measured wind fluctuations are directly recovered by these analyses.

We estimate the rotation correction at a grid point for each of the three seasons by calculating complex inner correlation coefficients between the calculated wind at that point and all available measured winds that are within ± 90 km alongshore and have at least 50% good data. The inner phases of the complex correlation coefficients, which measure the average misalignment between fluctuations of two vector series [*Kundu*, 1976], are then averaged over all measurement stations near each grid point where the winds are significantly correlated with the calculated wind. At least one good measurement station is available near grid points 2 through 17, excluding point 14 (Figure 2). Since we rotate calculated winds by the negative of the inner phase to align with measured winds, we refer to the negative of these averaged inner phases as the rotation correction for calculated winds.

The rotation corrections calculated here have values similar to those calculated for summer 1973 [*Halliwell and Allen*, 1984], and the estimates along the British Columbia coast are

TABLE 2. Wind Measurement Stations

Station	Abbreviation	North Latitude	West Longitude	y, km	Coast Orientation	Time Periods Used
Stations Used in Analysis of Wind Field Properties						
Cape St. James, B. C.*	CSJ	51°56′	131°01′	1760	115	all
Cape Scott, B. C.*	CSC	50°47′	128°26′	1467	134	winter 1981–1982, summer 1982
Quillayute, Wash.*	QUI	47°57′	124°32′	1055	110	all
Grays Harbor, Wash.*	GRH	46°55′	124°06′	936	95	all
Newport, Oreg.*	NEW	44°38′	124°03′	683	82	all
North Bend, Oreg.	NOB	43°25′	124°15′	547	73	all
Crescent City, Calif.	CCY	41°47′	124°14′	362	103	all
Humboldt Bay, Calif.	HUM	40°46′	124°14′	246	75	summer 1981
NDBC 46022	B22	40°46′	124°31′	240	75	winter 1981–1982, summer 1982
NDBC 46014*	B14	39°13′	123°58′	71	100	summer summer 1982
Point Arena Light, Calif.	ARL	38°57′	123°44′	41	110	winter 1981–1982
NDBC 46013	B13	38°14′	123°18′	−61	133	all
NDBC 46012*	B12	37°22′	122°39′	−171	105	all
Point Sur, Calif.	SUR	36°18′	121°53′	−301	115	all
Diablo Canyon, Calif.*	DIA	35°14′	120°50′	−464	120	winter 1981–1982
NDBC 46011*	B11	34°53′	120°52′	−506	90	summer 1981, summer 1982
Point Mugu, Calif.*	MUG	34°07′	119°07′	−678	155	all
San Diego, Calif.*	SDO	32°44′	117°10′	−936	105	all
Additional Stations						
Hoquiam, Wash.	HOQ	46°58′	123°56′	942	95	
Point St. George, Calif.	PSG	41°47′	124°16′	362	103	
Arcata, Calif.	ACA	40°59′	124°06′	270	75	
Sea Ranch	SRA	38°41′	123°26′	0	133	
CODE Meteorological Buoy C3	C3	38°36′	123°28′	0	133	
Bodega Marine Laboratory	BML	38°19′	123°04′	−46	133	
Pillar Point, Calif.	PIL	37°30′	122°30′	−156	105	
Pigeon Point, Calif.	PIG	37°11′	122°24′	−191	102	

Additional stations were used to fill data gaps (section 2.2) and to compare land and offshore winds (section 3.4). Coast orientation is measured in degrees anticlockwise from due east. NDBC stands for National Data Buoy Center.

*Stations from which data are plotted in Figures 3 and 5.

consistent with the observations of *Thomson* [1983]. They are positive throughout the CODE large-scale domain in all three seasons, indicating that calculated winds must be rotated anticlockwise, and they fluctuate in magnitude between about 5° and 50° over alongshore scales of a few hundred kilometers (Figure 2). Seasonal differences are small, so we average the rotation corrections for all three seasons at each grid point (Figure 2, right panel) then rotate the calculated winds by these averaged angles. For grid point 14 we linearly interpolate the correction between points 13 and 15 (Figure 2). For grid points 32 to 35 and 1, we use the correction angle of 45°, which is approximately the average observed within the Southern California Bight at points 2 and 3. Because of this uncertainty in the correction along the Baja California coast, we do not use calculated alongshore winds equatorward of grid point 2 in any analyses that quantify the space-time properties of the wind fields throughout the CODE large-scale domain.

3. Basic Statistical Properties of the Wind Field

3.1. *Seasonal Means*

In summer, calculated and measured wind vector means (Figure 3) point primarily alongshore and equatorward south of the Oregon-Washington border (46°N). During summer 1981 they point increasingly onshore with increasing y poleward from this border, pointing almost directly onshore at the northern end of the CODE large-scale domain. This anticyclonic mean flow pattern essentially outlines the northeastern and eastern side of the North Pacific subtropical high. During summer 1982 the vector means point approximately alongshore and equatorward everywhere along the coast, primarily because the subtropical high extends farther to the north on average than it did during summer 1982 (section 5). Measured and calculated wind vector means point in roughly the same direction throughout the domain, except in the Southern California Bight (32° to 34.5°N). Calculated wind vector means tend to vary smoothly along the coast in both amplitude and direction, while those for measured wind vary more irregularly. Both wind sets have the largest vector mean amplitudes $(\langle u\rangle^2 + \langle v\rangle^2)^{1/2}$, where angle brackets denote time average, along the California coast south of Cape Mendocino (40°N), with the exception of measured winds in the Southern California Bight.

The summer calculated alongshore wind means (Figure 4) are relatively large and negative (equatorward) along nearly the entire California coast ($-1000 < y < 400$ km), while the same is true for the measured winds only between Cape Mendocino ($y \approx 200$ km) and Point Conception ($y \approx -550$ km). These maxima are more distinct during summer 1981 than during summer 1982. The measured means are sharply re-

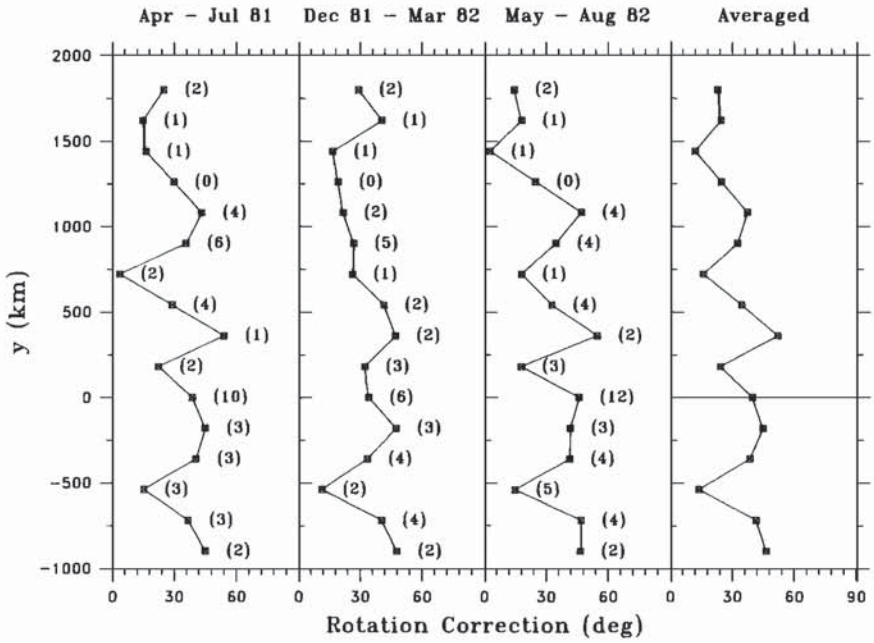

Fig. 2. The rotation correction required to align the calculated wind fluctuations with measured wind fluctuations for grid points 2 through 17 for the three seasons. A positive correction means that the calculated winds must be rotated anticlockwise to be aligned with the measured winds. The number of measurement stations avaiable near each grid point is in parentheses.

duced in the Southern California Bight ($-1000 < y < -550$ km) compared to those poleward of the bight in both summers. The mean equatorward alongshore wind tends to decrease less rapidly with increasing y poleward of California ($y > 400$ km) during summer 1982 because the subtropical high extends farther to the north on average than it did during summer 1981 (compare Figure 3).

In winter the directions of calculated and measured vector means point northward (southward) to the north (south) of the CODE experimental site (Figure 3). The calculated wind vector mean amplitudes exceed those of the measured wind everywhere except near the latitude of the reversal. The measured wind vector mean amplitudes are generally smaller in winter than in summer throughout the domain, but those of the calculated winds are larger in winter than in summer to the north of the California-Oregon border (42°N). The measured and calculated wind vector means tend to point in the same direction throughout the domain, including the Southern California Bight (32° to 34.5°N). A major winter discrepancy exists near station CSJ (52°N), where the CSJ mean points toward the east while the calculated wind mean at grid point 17 is substantially stronger and points toward the northwest.

The measured alongshore wind means in winter change sign near the site of the CODE experiment, while calculated means change sign about 200 km equatorward of the site (Figure 4). The calculated means change gradually between the California-Oregon border ($y \approx 400$ km) and northern Baja California ($y < -1000$ km), but the measured means change sign more abruptly near the CODE site. Measured means are substantially smaller than calculated means except near the location of the wind reversal. Unlike in summer, measured means within the Southern California Bight ($-1000 < y < -550$ km) are similar to measured means poleward of the bight.

3.2. *Seasonal rms Amplitudes*

In summer, rms principal axis ellipses (Figure 5) demonstrate that the measured wind fluctuations are strongly polarized in the alongshore direction, with the greatest polarization located along the California coast poleward of Point Conception (34.5°N to 42°N). The calculated winds (unrotated) are sustantially less polarized, but the major axes still have some tendency to align along the coast. The calculated wind ellipses would have to be rotated anticlockwise to align with the measured wind ellipses at most locations along the shelf, which is consistent with the statistically determined misalignment between calculated and measured wind fluctuations (Figure 2). One notable exception to this is at station NEW (44.6°N) (Figure 5), where the major axis of the measured wind has a substantial across-shelf component, possibly due to local topography in the Yaquina Bay area. However, caution must be exercised in comparing measured and calculated wind principal axis ellipses, since measured winds are constrained to fluctuate primarily in the alongshore direction by coastal mountain barriers, while calculated winds are not. The calculated wind vector rms amplitudes $[\langle (u - \langle u \rangle)^2 \rangle + \langle (v - \langle v \rangle)^2 \rangle]^{1/2}$ generally decrease from north to south by a factor of 2 within the large-scale domain, which is a pattern substantially different from that of the mean wind (Figure 3). (We hereinafter refer to wind rms amplitude simply as wind amplitude.) The measured wind vector amplitudes vary more irregularly along the coast and are relatively large between Cape Mendocino (40°N) and Point Conception (34.5°N) during both summers.

The summer calculated alongshore wind amplitudes (Figure 4) decrease by nearly a factor of 3 from north to south. A relative maximum exists near Cape Mendocino ($y \approx 200$ km) during summer 1982. For measured alongshore winds the amplitudes are relatively large between Cape Mendocino and

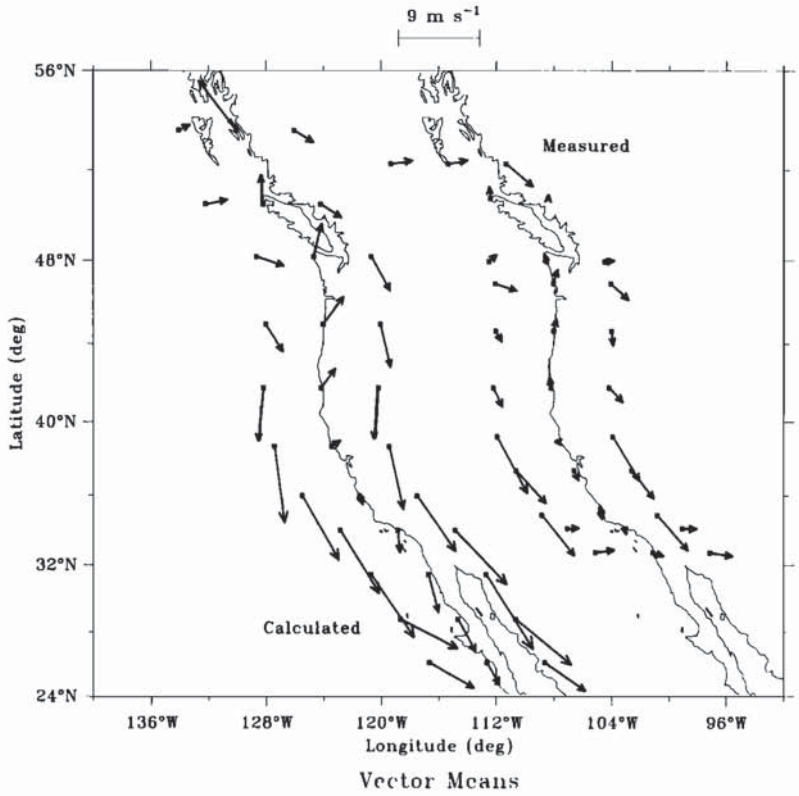

Fig. 3. Mean vectors for calculated (left coastline) and measured (right coastline) winds. For each coastline the vectors to the left are for April–July 1981, the vectors at the coast are for December 1981 through March 1982, and the vectors to the right are for May–August 1982. The origins of the vectors are at the appropriate CODE grid point or measurement station. The mean vectors for the summer seasons are displaced $\pm 4°$ longitude from each coast. Calculated wind means are shown for every other grid point centered at point 7 (the CODE site). Measured wind means are shown for most stations (see Table 2). The calculated winds have not been rotated. The longitude axis is correct for the left coastline.

Point Conception ($y \approx -550$ km). They are larger than those for calculated winds within this subdomain in both summers, but the difference is substantially larger in summer 1982. Outside of this subdomain the measured wind amplitudes are about equal to or less than those of the calculated winds, except at CSJ ($y = 1760$ km).

In winter, the measured and calculated wind fluctuations are substantially less polarized than in summer (Figure 5), resulting largely from the passage of stronger synoptic-scale atmospheric systems (section 5) that can drive stronger across-shore winds past the coastal mountain barrier. The measured wind major axes are oriented in the alongshore direction, except at NEW (44.6°N), where the orientation is the same as in summer, and at station GRH (46.9°N), where the across-shore winds are more energetic than the alongshore winds, probably because of the relatively low coastal mountain barrier at that location. Other than at GRH, there is generally little difference between winter and summer in both the measured and calculated wind major axis orientations. As in summer, the calculated winds are less polarized than the measured winds, and the major axes of the calculated wind ellipses tend to be rotated clockwise from those of the measured winds. The calculated wind vector amplitudes are larger than those of the measured wind everywhere, are larger everywhere in winter than they are in summer, and decrease by a factor of 3 from north to south, with most of the decrease occurring equatorward of Cape Mendocino (40°N). Measured wind vector amplitudes have a relative maximum between Cape Mendocino and Point Conception (34.5°N), which was also observed for the two summers.

The winter calculated alongshore wind amplitudes (Figure 4) decrease from north to south by a factor of 3 between the relative maximum centered near Cape Mendocino ($y \approx 200$ km) and the southern end of the CODE large-scale domain. The measured wind amplitudes are relatively large between Cape Mendocino and Point Conception ($y \approx -550$ km), where they approximately equal those of the calculated winds. Elsewhere, the measured wind amplitudes are substantially smaller than those of the calculated winds, except at CSJ ($y = 1760$ km).

3.3. *The Coastal Boundary Layer Influence on Wind Properties*

The mean and rms amplitude of coastal measured wind fluctuations vary considerably over scales small in comparison with synoptic-scale atmospheric pressure systems. Most of this variability can be attributed to several coastal atmospheric boundary layer processes, not all of which are independent. We now qualitatively discuss the effects of these processes, and how they probably contribute to the observed differences in measured and calculated wind statistics.

The coastal mountain blocking causes wind measurements to be strongly polarized in the alongshore direction. Although they are not directly affected by this blocking, calculated winds are still polarized in roughly the alongshore direction after the additional boundary layer rotation is made (section

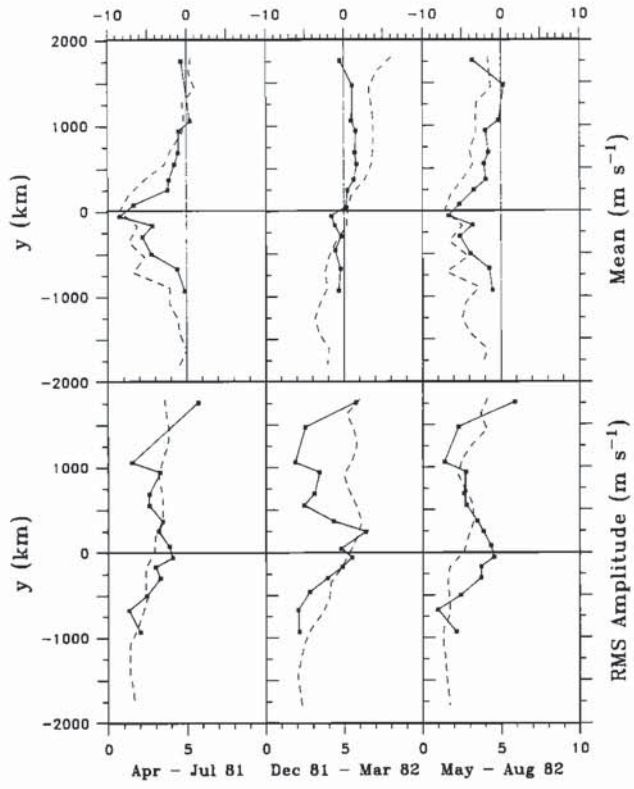

Fig. 4. The means and rms amplitudes of the calculated (dashed) and measured (solid) alongshore winds as a function of y for the three seasons.

2.2), but not as strongly as measured winds. Other processes may therefore contribute to the preference for alongshore polarization. For example, surface isobars in summer tend to parallel the coast between the subtropical high and thermal low (see section 5), so fluctuations in the strength of these systems will cause wind to fluctuate primarily in the alongshore direction. However, calculated winds remain slightly polarized in the alongshore direction in winter, so this seasonal pattern does not fully explain the polarization.

The presence of coastal mountains and a stratified atmosphere allows pressure and wind fluctuations to exist at scales substantially smaller than those of synoptic-scale systems. For example, poleward propagating coastally trapped pressure fluctuations with across-shore scales of 100–200 km [*Dorman*, 1985, this issue; *Mass et al.*, 1986] can exist, the effects of which we discuss in sections 4 and 5. Other dynamical processes permit the existence of pressure and wind fluctuations that have spatial scales equal to or smaller than the shelf width [$O(1)$ to $O(10)$ km]. For example, *Beardsley et al.* [this issue] and *Friehe and Winant* [1982, 1984] observe changes in wind speed of more than a factor of 3, and changes in wind direction of more than 20°, over spatial separations of several kilometers on the continental shelf at the CODE site during CODE 1 and CODE 2. Also, when the spring-summer equatorward winds blow, some regions of relatively strong or weak winds tend to persist in the same locations. Consequently, the amplitude of measured wind fluctuations is probably sensitive to small changes in the location of a station.

The measured wind data set consists of a mixture of coastal land stations and offshore buoys, and three boundary layer processes may contribute to differences between these winds. Surface friction is larger over land than over water, so the measured land winds at the coast will tend to have smaller amplitude than those over water. Also, the topography at the coast may locally steer the wind, affecting both speed and direction. *Brink et al.* [1984] note that winds at the coast near Point Conception ($y \approx -550$ km) tend to be stronger near headlands than at other alongshore locations. Finally, the diurnal (land breeze–sea breeze) cycle can influence daily-averaged wind velocity, since the daytime sea breeze and nighttime land breeze speeds are usually not equal, and this will affect seasonal mean winds. Low-frequency wind fluctuations may be affected, since low-frequency changes in the strength of the diurnal cycle exist at the CODE site [*Beardsley et al.*, this issue]. The diurnal cycle at the CODE site is strong at coastal land stations but weak at buoys on the outer continental shelf and may therefore contribute to the observed differences between land and offshore winds. We therefore expect that the observed alongshore changes in measured wind statistics are influenced by the mixture of land stations and offshore buoys.

With so many processes influencing measured winds within the coastal atmospheric boundary layer, measured wind amplitudes differ substantially from those of calculated winds at many locations along the coast, and it is difficult to determine a consistent alongshore distribution of wind amplitude. For example, relatively large measured wind amplitudes exist in both summer and winter between Cape Mendocino ($y \approx 200$ km) and Point Conception ($y \approx -550$ km), but this regional maximum does not appear in the calculated winds. This maximum may be partly enhanced in all seasons because most of the measurements in this region are from offshore buoys. However, the few coastal stations in the region (SUR for all three seasons and ARL and DIA during winter 1981–1982) all have larger fluctuations than the coastal stations outside of the region, indicating that this maximum in the measured wind field is at least partly real. Also, the dominance of land stations in the northern part of the CODE large-scale domain may be at least partly responsible for the reduced measured wind amplitudes there. For example, station QUI ($y = 1055$ km), where wind amplitude is relatively small, is located several kilometers inland.

3.4. *Can Land Winds be Adjusted to Equal Offshore Winds?*

We determine if it is possible to adjust winds at land stations to equal winds offshore. On the basis of land and sea wind measurements from several coastal regions (not including the continental shelf in the CODE large-scale domain), *Hsu* [1981, 1986] recommends that coastal land vector wind speed be adjusted by the following formula to represent offshore vector wind speed:

$$\hat{U}_o = 1.62 + 1.17U_l \tag{1}$$

where U_l is the measured land speed and $\hat{U}_o$ is the estimated offshore speed, all in units of meters per second. This relationship is tested in all three seasons by regressing offshore buoy wind speed on nearby coastal wind speed in the CODE large-scale domain (Table 3). The additional stations used in this comparison are listed in Table 2. The regression coefficients vary substantially between summer and winter and also between both summers. Calculating the mean of all regression coefficients listed in Table 3, we obtain

$$\hat{U}_o = 2.19\ (\pm 1.35) + 1.00\ (\pm 0.38)U_l \tag{2}$$

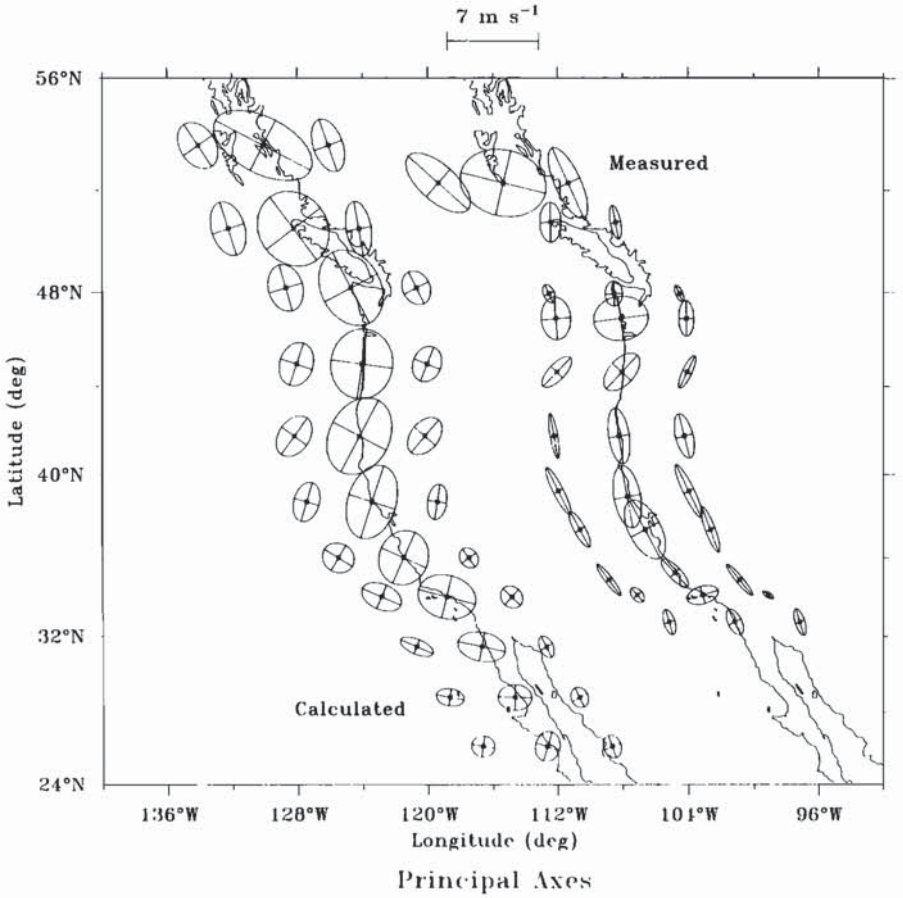

Fig. 5. Same as Figure 3, except for rms principal axis ellipses.

with the standard deviations given in parentheses, and with $\hat{U}_o$ and U_l given in meters per second. Although these coefficients are statistically indistinguishable from those recommended by *Hsu* [1986], we do not correct our coastal land winds using this formula because of both the large uncertainty in the coefficients and the apparent variability of the coefficients in space and time.

We also test if we can simply adjust the rms amplitudes of coastal land alongshore winds by a constant factor to represent offshore alongshore winds. A tabulation of the ratios of the alongshore wind amplitudes at offshore stations to those of nearby coastal land stations for the three seasons (Table 3) reveals that they also vary with both alongshore location and time. For example, near Point Conception (represented by station pair B11-DIA), wind amplitude is slightly smaller offshore in summer and larger offshore in winter, and the ratio is

TABLE 3. Regression of Offshore Vector Wind Speed U_o on Nearby Land Vector Wind Speed U_l, $\hat{U}_o = a + bU_l$, and the Variance Ratio of Buoy Alongshore Winds to Nearby Land Alongshore Winds

Time Interval	Station		Regression Coefficient m s^{-1}		Correlation Coefficient	rms Amplitude Ratio	Common Good Data, %
	Buoy	Land	a	b			
April–July 1981	B14	ARL	1.21	1.08	0.76	1.22	100
	C3	SRA	2.93	1.05	0.81	1.26	88
	B13	BML	5.30	0.86	0.62	1.35	100
	B12	PIL	2.88	0.50	0.68	1.07	81
	B11	DIA	1.71	0.93	0.89	0.97	89
Dec. 1981–March 1982	B22	HUM	3.27	0.66	0.50	1.76	95
	B14	ARL	1.01	1.12	0.90	1.36	87
	C3	SRA	3.60	0.95	0.55	1.43	39
	B12	PIL	3.38	0.39	0.59	1.07	89
	B11	DIA	2.51	0.88	0.79	1.20	15
May–Aug. 1982	B22	HUM	0.26	1.49	0.72	1.74	95
	B14	ARL	0.59	1.25	0.80	1.27	100
	C3	SRA	1.42	1.98	0.85	2.14	70
	B13	BML	2.63	1.13	0.70	1.57	100
	B12	PIL	1.64	0.78	0.76	1.38	98
	B11	DIA	0.76	0.93	0.88	0.80	100

smaller during summer 1982 than summer 1981. In contrast, the wind amplitudes along the California coast between Monterey and the CODE site (represented by station pairs C3-SRA, B13-BML, and B12-PIL) are larger offshore during all seasons, and the ratios are substantially larger during summer 1982 than during both summer 1981 and the intervening winter, especially near the CODE site (C3-SRA). As a result, we cannot simply adjust coastal land alongshore wind amplitudes by a constant factor to represent offshore alongshore winds.

The inability to devise a simple correction for land winds may be caused by factors such as the large-amplitude, small-scale structure observed in the wind field [*Beardsley et al.*, this issue] and the topographic influence on coastal land winds. The small-scale structure may have a seasonal cycle caused by seasonal cycles in synoptic-scale atmospheric variability and in the properties of the coastal marine boundary layer.

3.5. *Effects of the rms Amplitude Distribution on Statistical Analyses*

The different representations of wind amplitude along the coast provided by the measured and calculated wind fields can have a major effect on some statistical analyses. Consider a true wind field $v(y, t)$, with zero mean at all y and the rms amplitude distribution $s(y) = \langle v^2(y, t)\rangle^{1/2}$. Now consider a sample of this wind field, $\hat{v}(y, t)$, that differs from the true field only in rms amplitude distribution $\hat{s}(y) = \langle \hat{v}^2(y, t)\rangle^{1/2}$. The sampled wind field is then given in terms of the true field by $\hat{v}(y, t) = \xi(y)v(y, t)$, where $\xi(y) = \hat{s}(y)/s(y)$. The function $\xi(y)$ represents the y-dependent error ratio in the rms amplitudes of the sampled wind field, which differs substantially between the calculated and measured wind fields. These amplitude errors will affect the results of many of our statistical analyses, and since we cannot correct for them, we must attempt to understand how they influence the interpretation of these analyses.

We employ the following strategy to accomplish this: We form an additional data set by adjusting the measured wind amplitude at each station to equal the calculated wind amplitude at that alongshore location. Defining the mean measured alongshore winds as

$$\bar{v}_m(y) = \langle v_m(y, t)\rangle \tag{3}$$

we then define

$$v_a(y, t) = \xi_{cm}(y)[v_m(y, t) - \bar{v}_m(y)] + \bar{v}_m(y) \tag{4}$$

with

$$\xi_{cm}(y) = \frac{s_c(y)}{s_m(y)} \tag{5}$$

where v_m and v_a are the measured and adjusted measured winds, and s_c and s_m are the calculated and measured wind rms amplitudes. We linearly interpolate s_c alongshore to the location of the measurement stations. We use the vector rms amplitude $[\langle(v_e - \langle v_e\rangle)^2\rangle + \langle(v_n - \langle v_n\rangle)^2\rangle]^{1/2}$, where v_e and v_n are east and north wind components, to calculate $\xi_{cm}(y)$ for adjusting vector winds. We also form additional data sets by normalizing both the measured and calculated winds to unit amplitude. Analyses are performed for measured winds, adjusted measured winds, normalized measured winds, calculated winds, and normalized calculated winds. The results of these analyses are then compared to determine what part represents true features of the wind field and what part represents the influence of changes in the alongshore distribution of wind amplitude. For all analyses, we present the results for measured and calculated winds. For the analyses influenced by wind amplitudes, we also present the results for adjusted measured winds, and we occasionally present the results for normalized winds. Adjusting measured wind amplitudes to equal those of calculated winds does not mean that we believe calculated winds better represent the true wind amplitudes along the coast. We do this only to assess the impact of changing the alongshore distribution of wind amplitude, and hence the impact of rms amplitude errors in the calculated and measured wind sets, on our analyses.

3.6. *Correlation Scales and Wind Field Correlations*

We use the space- and time-averaged correlation function to estimate integral correlation space and time scales. For a wind field sampled at N evenly spaced points, $v(y_i, t)$, $i = 1, N$, this function is given by

$$R(\eta_n, \tau) = \frac{\sum_{i=I}^{J} \langle v(y_i, t)v(y_i + \eta_n, t + \tau)\rangle}{\left[\sum_{i=I}^{J} \langle v^2(y_i, t)\rangle\right]^{1/2}\left[\sum_{i=1}^{J} \langle v^2(y_i+\eta_n, t+\tau)\rangle\right]^{1/2}} \tag{6}$$

where

$$\begin{aligned} &I = 1, \quad J = N - n \qquad n \geqq 0, \\ &I = |n| + 1, \quad J = N \qquad n < 0, \quad |n| \leqq |N - 1| \end{aligned} \tag{7}$$

η_n is the lag distance, and τ is the lag time. To calculate the integral correlation time scale, the function $R(0, \tau)$ is integrated over $\tau \geqq 0$ out to the first zero crossing of R. For the space scale, $R(\eta_n, 0)$ is integrated over η_n for $n \geqq 0$ out to the first zero crossing of R. We use measured winds interpolated to the CODE grid points (section 2.1) in this analysis.

The correlation time scales (Table 4) between grid points 4 and 13 typically range between 1 and 2 days. This alongshore subdomain is selected to avoid both the Southern California Bight and the poor alongshore resolution of measured winds along the British Columbia coast. The scales are similar for summer 1981 and winter 1981–1982 but are substantially larger for summer 1982. Calculated winds tend to have slightly larger time scales than measured winds. Adjusting or normalizing measured wind amplitudes and normalizing calculated wind amplitudes causes only small changes in the estimated time scales. The correlation space scales (Table 4) are typically 400 to 800 km in summer and 600 to 1000 km in winter, showing the dominance of large scales in the wind fluctuations. Calculated wind space scales exceed the measured wind scales by about 60% during all three seasons, presumably because of the poor representation of smaller-scale wind fluctuations by the calculated winds. However, even the measured wind space scales exceed the typical station spacing by a substantial margin (Figure 1, Table 2), indicating that we have sampled the measured winds at sufficiently small alongshore intervals to resolve the large-scale fluctuations. Winter space scales exceed summer scales by about 20%, and changes in the space scales due to adjusting or normalizing the time series are relatively small.

The zero time-lagged spatial correlation matrices of calculated and measured alongshore winds (Figure 6) illustrate the alongshore dependence of spatial correlation scales. The hori-

TABLE 4. Integral Correlation Alongshore Space Scales and Time Scales for Coastal Alongshore Winds Between Grid Points 4 (34.6°N; $y = -540$ km) and 13 (48.2°N; $y = 1080$ km)

	Integral Correlation Scale					
	April–July 1981		Dec. 1981–March 1982		May–Aug. 1982	
Wind Field	Space, km	Time, days	Space, km	Time, days	Space, km	Time, days
Calculated	824	1.44	1036	1.36	746	2.06
Normalized calculated	776	1.56	1042	1.27	768	1.95
Measured	436	1.27	592	1.13	452	1.98
Adjusted measured	556	1.09	662	1.28	442	1.91
Normalized measured	474	1.20	658	1.19	496	1.80

zontal (vertical) axes represent the alongshore locations of the columns (rows) of the matrices. These locations are evenly spaced for the CODE grid points but not for the measurement stations. The locations of the rows and columns representing each station or grid point are shown by the tick marks on the diagonals of the matrices. To determine the correlation between a given station and stations to the south (north), start at the tick mark and follow a straight line vertically down (horizontally toward the left) from the mark. If the correlation contours bunch close to the diagonal at a given location, then winds poleward and equatorward of that location are poorly correlated with each other.

During both summers, the calculated wind correlation coefficients become insignificant (<0.35; see appendix) for spatial

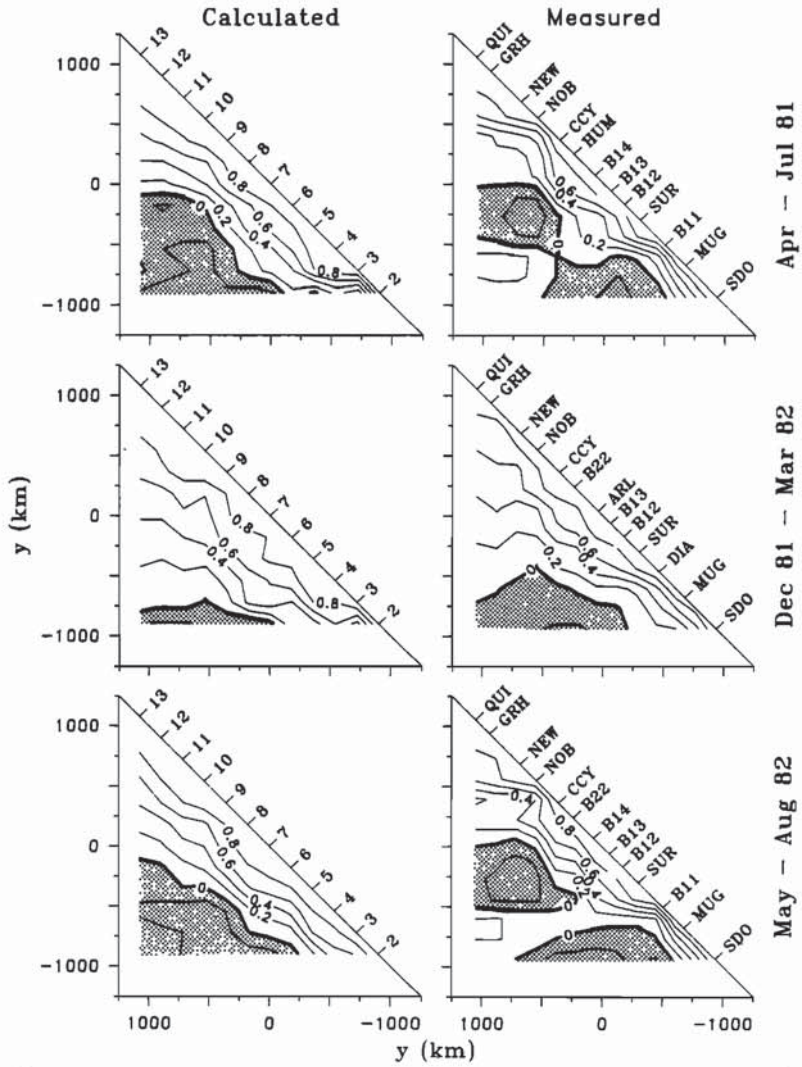

Fig. 6. Zero time-lagged correlation matrices for calculated and measured winds contoured as a function of alongshore separation. Correlation coefficients of >0.35 are statistically significant to be 95% level of confidence (see appendix). The matrices are calculated for the U.S. coast only, where measurement station spacing is relatively uniform. Negative correlations are shaded.

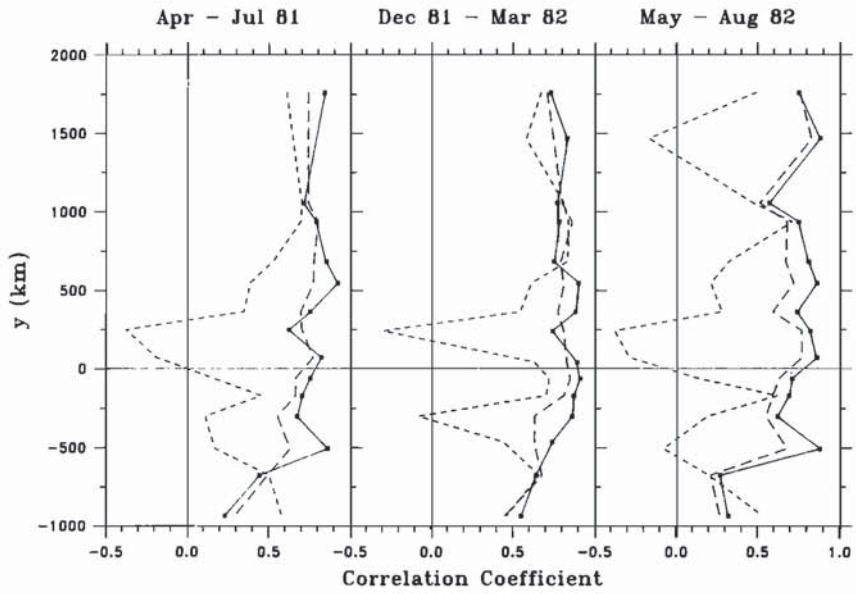

Fig. 7. Correlation coefficients between measured and calculated winds. The correlation coefficients of alongshore wind (solid lines), across-shore winds (short-dashed lines), and the inner correlation coefficients of vector winds (long-dashed lines) are plotted as a function of y for the three seasons. Correlation coefficients of >0.35 are statistically significant to a 95% level of confidence (see appendix).

separations averaging between 600 and 800 km, with a tendency for this scale to decrease from north to south. During winter the calculated wind correlation coefficients become insignificant over scales ranging from 1200 km in the north to 600 km in the south. In all seasons, correlations become insignificant over smaller spatial separations for the measured winds than for the calculated winds. The rate of decrease of correlation with spatial separation tends to vary more smoothly along the coast for calculated winds than for measured winds. The only exception to this is during summer 1981 and winter 1981–1982, where calculated winds at grid point 2 are poorly correlated with those poleward of that location, which is probably related to the large changes in coastline orientation there. During both summers, measured winds poleward of Point Conception ($y \geqq -550$ km) tend to be poorly correlated with those equatorward, consistent with our observations that winds behave differently in the Southern California Bight ($-1000 < y < -550$ km). Also, measured winds poleward of the California-Oregon border ($y \geqq 400$ km) tend to be poorly correlated with those equatorward.

The amplitude of the inner correlation coefficients between measured and calculated vector winds, and the correlation coefficients between measured and calculated alongshore winds (Figure 7), are statistically significant (>0.35; see appendix) throughout the large-scale domain in all seasons, except in the Southern California Bight during summer where only station MUG ($y = -678$ km) vector and alongshore winds in 1981 are significantly correlated with the calculated winds. The alongshore winds tend to be slightly better correlated than the vector winds in all seasons, and these correlations are slightly smaller during summer 1982 than summer 1981. The phases of the vector inner correlations (not shown) are consistent with the misalignment discussed in section 2.2. The across-shore wind correlations (Figure 7) are substantially smaller in magnitude than the alongshore wind correlations in all seasons, except along the Washington coast (near $y = 1000$ km) in summer, along the Washington and Oregon coasts in winter, and in the Southern California Bight ($-1000 < y < -550$ km) in summer. Along the California coast outside of the bight ($-550 < y < 400$ km), the alongshore components are much better correlated than the across-shore components during both summer and winter, probably owing to the blocking of the across-shore components by relatively tall coastal mountains. Within the bight, however, the across-shore components of the two wind sets are better correlated than the alongshore components.

3.7. *The Coastal Boundary Influence on Alongshore Wind Statistics*

After correcting the calculated geostrophic winds for the boundary layer rotation, good correlations are observed between calculated and measured alongshore winds poleward of the Southern California Bight ($y \geqq -550$ km). This result indicates that the coastal boundary layer primarily influences the rms amplitude of the fluctuations. In contrast, the quality of the across-shore wind component is severely affected by the coastal boundary in most of the large-scale domain, but it is probably not important in driving large-scale coastally trapped waves.

Strong coastal boundary effects must be present in the Southern California Bight in summer, since mean measured alongshore winds differ substantially from mean calculated alongshore winds, and since measured and calculated alongshore winds are poorly correlated with each other. Measured and calculated across-shore winds are better correlated than alongshore winds there. This indicates that summer measured winds in the bight are not closely related to gradients of the synoptic-scale atmospheric pressure field. The coastal mountains abruptly turn from a north-south to an east-west orientation near Point Conception ($y \approx -550$ km), and the nearshore wind velocity consequently changes abruptly at this location [*Brink et al.*, 1984]. Another mechanism that could suppress the summer alongshore wind correlations is the "Catalina eddy" events in the wind field [*Bosart*, 1983]. These

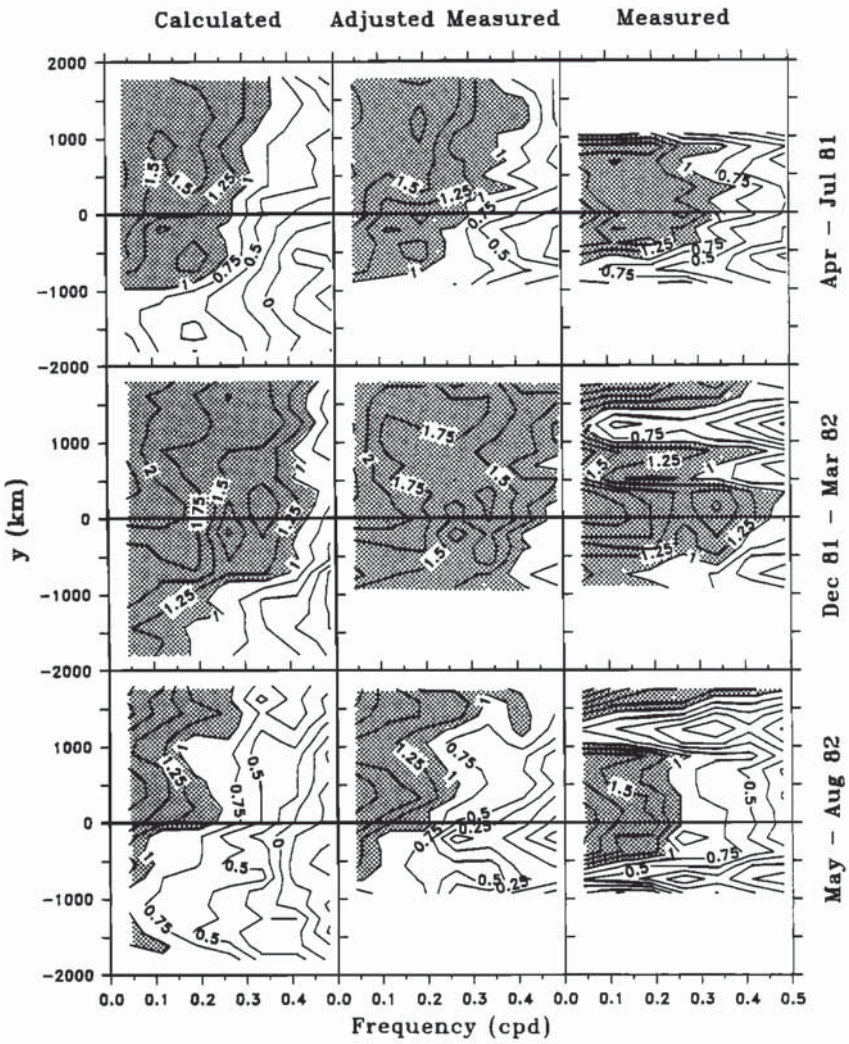

Fig. 8. Autospectra of calculated, adjusted measured, and measured alongshore winds for the three seasons. The contours are of $\log_{10}[S(y, \omega)]$, with S in units of $m^2\ s^{-2}\ cpd^{-1}$. The number of degrees of freedom is 18. The 95% confidence limits are between $\log_{10} S - 0.24$ and $\log_{10} S + 0.34$ at all y and ω. The autospectra are shaded where $S(y, \omega) > 10^1$. Autospectra for measured winds north of QUI ($y = 1055$ km) are not contoured for April–July 1981 owing to the large data gap between QUI and CSJ ($y = 1760$ km). The frequencies at which spectrum estimates exist are shown in Figure 14.

cyclonic wind eddies essentially fill the entire bight over time intervals of around 2 days and produce poleward alongshore coastal winds within the bight at the same time that equatorward alongshore coastal winds exist poleward of Point Conception. If these mesoscale wind eddies and the resulting coastal alongshore wind reversals within the bight are not well represented in the calculated wind field, the correlation coefficients between measured and calculated alongshore winds within the bight could be reduced as was observed (see section 5). The influence of the bight is not as great in winter, when relatively strong propagating pressure systems drive the wind field there.

4. Spectrum Analysis of the Wind Field

4.1. *Frequency Domain Properties*

We study the frequency domain properties of the wind field using autospectrum and cross-spectrum analysis of calculated, measured, and adjusted measured winds. We discuss autospectra $[S(y, \omega)]$ of alongshore winds (Figure 8), the rotary coefficients $[S_r(y, -\omega) - S_r(y, +\omega)]/[S_r(y, +\omega) + S_r(y, -\omega)]$, where S_r indicates rotary autospectrum [*Gonella*, 1972; *Mooers*, 1973] of vector winds (Figure 9), coherences between measured and calculated vector and alongshore winds (Figure 10), and spatial coherence scales of alongshore winds (Figure 11). The total rotary autospectra $S_r(y, +\omega) + S_r(y, -\omega)$ are not presented because the spectral shapes are very similar to those for alongshore wind.

Both the calculated and adjusted measured alongshore winds have similar distributions of variance density in (y, ω) space in all three seasons (Figure 8). They are red throughout the large-scale domain and have no distinct maxima or minima in summer 1982. In most of the alongshore subdomain $y > -1000$ km during summer 1981, a relative minimum exists near 0.11 cycles per day (cpd) and a relative maximum exists near 0.19 cpd. In the alongshore subdomain $-500 < y < 500$ km during winter 1981–1982, a relative minimum exists near 0.26 cpd and a relative maximum exists near

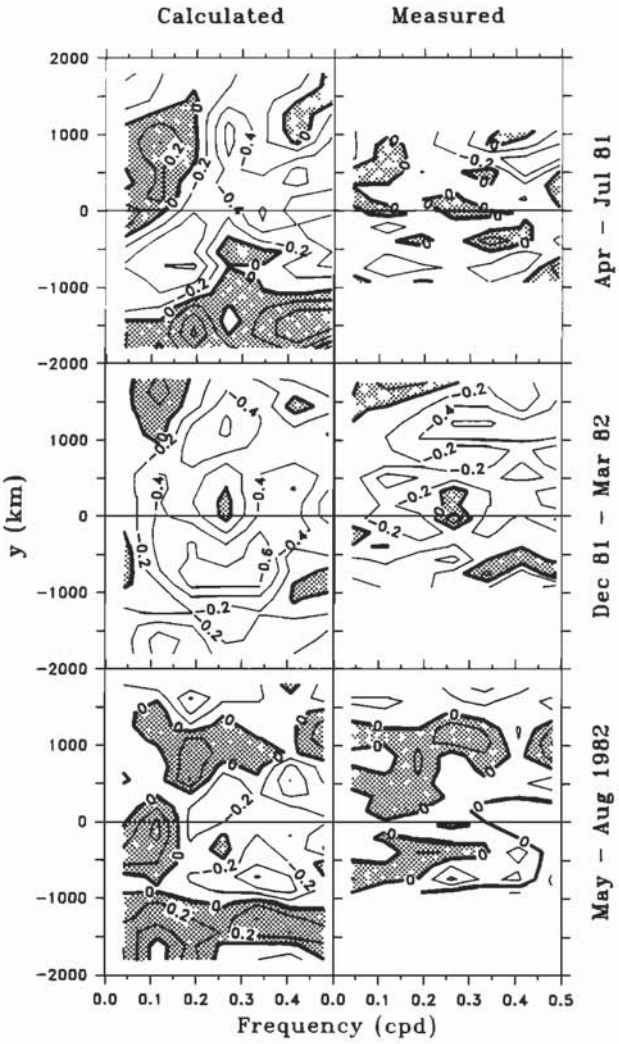

Fig. 9. Contours of rotary coefficients $[S_r(y, -\omega) - S_r(y, +\omega)]/[S_r(y, -\omega) + S_r(y, +\omega)]$ for calculated and measured vector winds for the three seasons. The coefficients for adjusted measured winds are identical to those for measured winds. Positive coefficients (anticyclonic variance exceeds cyclonic) are shaded. A rotary coefficient of +1 (−1) indicates that cyclonic (anticyclonic) variance is zero. The frequencies at which estimates exist are shown in Figure 14.

0.34 cpd. The variance density generally decreases from north to south at all frequencies in all seasons, with almost all of the winter decrease occurring equatorward of Cape Mendocino ($y < 200$ km). The calculated wind variance density increases toward the south along the Baja California coast ($y < -1000$ km) in both summers. Wind variance is largest in winter and is larger in summer 1981 than in summer 1982. Wind autospectra tend to be more red in summer 1982 than in either summer 1981 or winter 1981–1982, in agreement with the larger integral correlation time scales observed.

Some minor differences are observed, however, between the spectral shapes of calculated and adjusted measured alongshore winds in all seasons (Figure 8). We test the hypothesis that the true adjusted measured wind spectrum estimates $S_a(y, \omega)$ equal the true calculated wind spectrum estimates $S_c(y, \omega)$. At each (y, ω), we form the null hypothesis $S_a = S_c$ then test it against the alternate hypothesis $S_a \neq S_c$. We use the statistical F test, since the estimates $\hat{S}_a$ and $\hat{S}_c$ are χ^2 random variables. Because adjusted measured wind estimates are calculated at the measurement stations, we use a cubic spline interpolation in the alongshore direction at each frequency to obtain estimates at the y locations of the CODE grid points. Applying the F test, we find that $\log_{10}\hat{S}_a$ must differ by at least 0.43 from $\log_{10}\hat{S}_c$ to reject the null hypothesis that $S_a = S_c$ to a 95% level of confidence. We find significant differences between S_a and S_c only within the Southern California Bight ($-1000 < y < -550$ km) in the two summers, and at the highest frequency resolved (0.49 cpd) along the remainder of the coast during winter 1981–1982 and summer 1982. Elsewhere in (y, ω) space, fewer significant differences are observed than would be expected by chance in all seasons. We conclude that poleward of the bight in summer and everywhere in winter, we cannot reject the hypothesis $S_a = S_c$ at frequencies ≤ 0.41 cpd, and the observed minor differences in spectral shapes are not statistically significant. This result agrees with the comparisons between calculated and measured wind autospectra for $\omega < 0.5$ cpd of *Thomson* [1983] for the British Columbia coast, *Hsueh and Romea* [1983] for the East China Sea, and *Rienecker and Mooers* [1983] for three open ocean NDBC buoys in the northeast Pacific.

The measured alongshore wind variance is relatively large both along the California coast poleward of Point Conception ($y > -550$ km) and at CSJ ($y = 1760$ km) during all seasons (Figure 8). The variance is substantially reduced along the Washington coast, primarily because of the relatively small variance at QUI ($y = 1055$ km). Despite the large changes in measured alongshore wind variance along the coast, the analysis above indicates that the spectral shape for these winds is not significantly different from that of the calculated alongshore winds poleward of the Southern California Bight for $\omega \leq 0.41$ cpd. This provides additional support for our contention that the coastal atmospheric boundary layer effects primarily change the variance of alongshore wind measurements without seriously distorting other temporal statistical properties.

From the rotary coefficients (Figure 9), cyclonic variance dominates the calculated vector wind fluctuations in winter when propagating synoptic-scale atmospheric systems are strong and pass the coast frequently (section 5). During summer 1981, cyclonic variance exceeds anticyclonic in most of (y, ω) space poleward of Baja California ($y > -1000$ km) at frequencies of >0.2 cpd, while during summer 1982 this is true only along the California and southern Oregon coast ($-1000 < y < 600$ km) at frequencies > 0.2 cpd. During both summers, cyclonic variance exceeds anticyclonic at CSJ ($y = 1760$ km) over nearly the entire frequency band. For measured winds, there is less preference for cyclonic rotation than in the calculated winds during winter, and there is little preference for either rotation direction during both summers. The suppression of across-shore winds by coastal mountains apparently inhibits the rotation preference that is imposed by the fluctuation surface atmospheric pressure gradients caused by synoptic-scale systems.

The squared coherences between measured and calculated alongshore and vector winds (Figure 10) are largest during winter, are larger during summer 1981 than during summer 1982, and are very small in the Southern California Bight ($-1000 < y < -550$ km) in summer. In winter, large alongshore wind coherence exists across the entire frequency band poleward of the Southern California Bight ($y > -550$ km), with the exception of the northern Oregon and southern Washington coast ($y \approx 900$ km), and coherence within the bight is not as small as in summer. Alongshore wind coher-

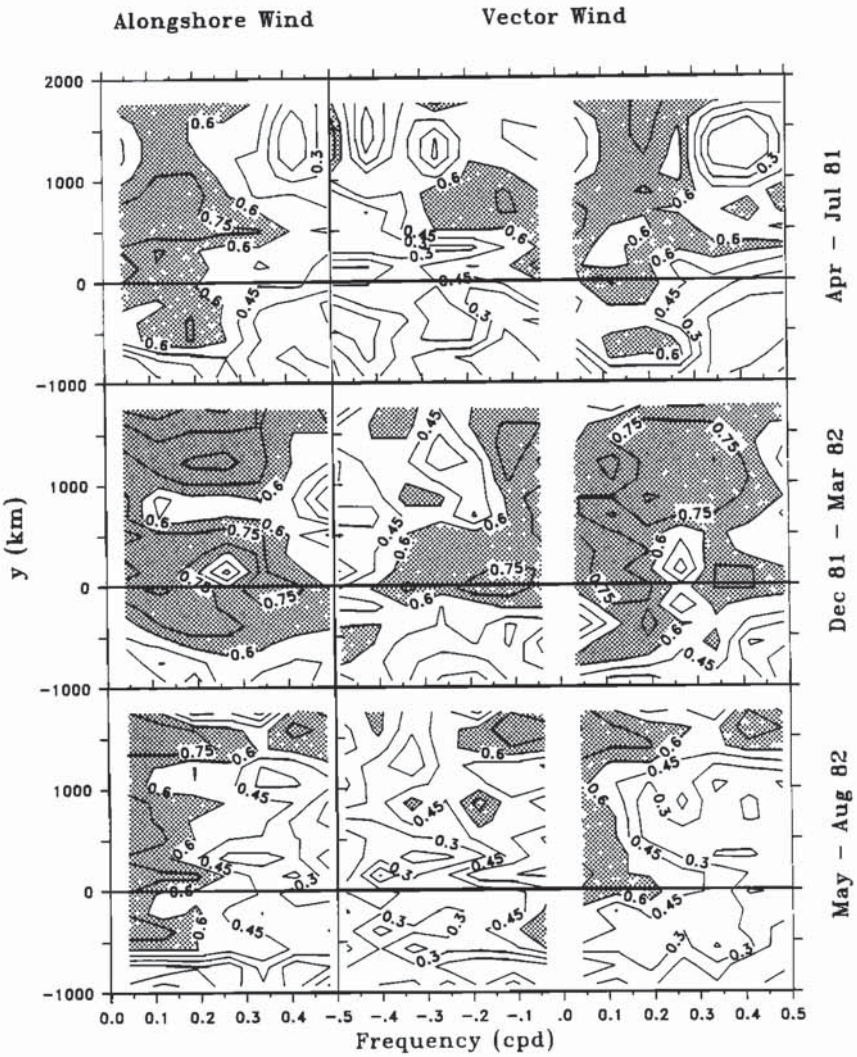

Fig. 10. The squared coherences between measured and calculated alongshore winds and squared rotary coherences between measured and calculated vector wind contoured as a function of frequency and y for the three seasons. Squared coherences greater than 0.6 are shaded, and those greater than 0.16 are statistically significant to a 95% level of confidence. The frequencies at which coherence estimates exist are shown in Figure 14.

ence decreases more rapidly with frequency during summer than during winter, and the summer decrease is more rapid during 1982. Coherence tends to be large in those parts of (y, ω) space where variance density is relatively large. For vector winds the squared rotary coherences tend to be larger for the cyclonic component ($+\omega$) than for the anticyclonic component in all three seasons, which may be related to the larger cyclonic variance that is observed primarily in the calculated winds.

During winter, relatively small coherence is observed between measured and calculated alongshore and vector (cyclonic component only) winds within ± 400 km of the CODE site near 0.26 cpd (Figure 10). The preference for cyclonic rotation in winter does not exist in this region of (y, ω) space (Figure 9). This reduced cyclonic variance produces a relative minimum in the contoured autospectra of both alongshore winds (Figure 8) and vector winds (not shown) and reduces the coherence between the cyclonic components of calculated and measured vector wind. We do not have a plausible explanation for this observation.

We use space-averaged squared coherence functions to estimate alongshore coherence scales as a function of ω. For a given wind field $v(y_i, t)$ sampled at N evenly spaced points, this function is given by

$$\gamma^2(\eta_n, \omega) = \left\{ \left(\left| \sum_{i=I}^{J} \{\bar{v}^*(y_i, \omega)\bar{v}(y_i + \eta_n, \omega)\} \right|^2 \right) \cdot \left[\left(\sum_{i=I}^{J} \{\bar{v}^*(y_i, \omega)\bar{v}(y_i, \omega)\} \right) \cdot \left(\sum_{i=I}^{J} \{\bar{v}^*(y_i + \eta_n, \omega)\bar{v}(y_i + \eta_n, \omega)\} \right) \right]^{-1} \right\} \quad (8)$$

where I and J are given by (7), the overbars denote Fourier transforms, the asterisks denote complex conjugate, and the brackets denote frequency band averaging. We calculate these functions over grid points 4 through 13 (Figure 11). Without spatial averaging, a γ^2 of 0.16 is statistically significant to a 95% level of confidence. At the maximum η_n (1260 km) the function is averaged over three points, or over an alongshore distance much smaller than the correlation space scales (Table 4). Since we gain no additional degrees of freedom by this

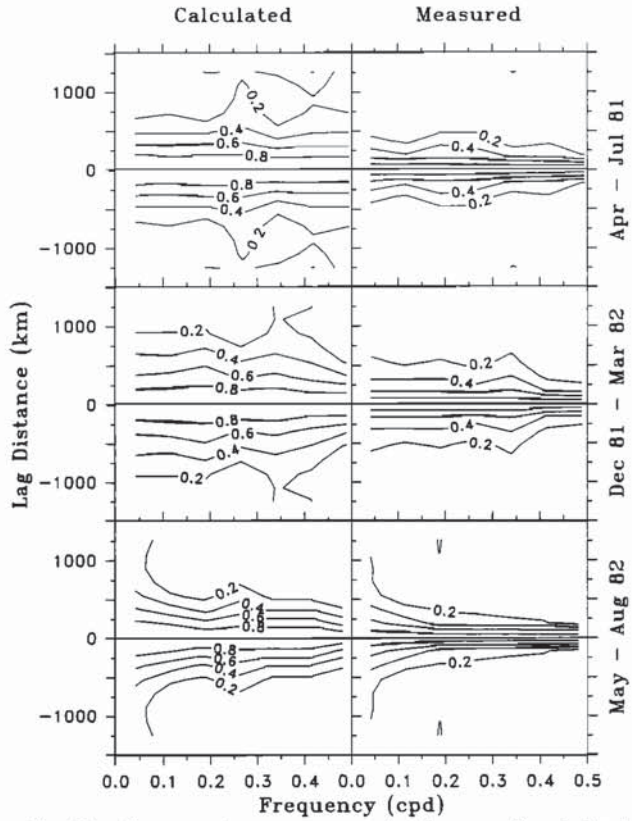

Fig. 11. The space-frequency squared coherence γ^2, calculated from space-averaged autospectra and cross-spectra (equation (8)) for calculated and measured alongshore winds over grid points 4 through 13 for the three seasons. The frequencies at which estimates exist are shown in Figure 14.

averaging, we estimate the coherence space scale as the alongshore separation at which the squared coherence decreases to 0.16. The calculated and measured wind coherence space scales tend to be either constant over all ω or decrease slightly with increasing ω. The scale equals or exceeds 1000 km for calculated winds during summer 1981 and winter 1981–1982 and for $\omega < 0.11$ cpd during summer 1982, while it is about 700 to 800 km for $\omega \geqq 0.11$ cpd during summer 1982. In contrast, the measured wind scales are substantially smaller than calculated wind scales in all seasons. The measured wind scale exceeds 1000 km only for $\omega = 0.041$ cpd in summer 1982. Otherwise, measured wind scales are typically between 400 and 600 km in summer and between 500 and 800 km in winter.

4.2. *Wave Number–Frequency Domain Properties*

We study the wave number–frequency (l, ω) domain properties of the alongshore wind field along the coast using autospectrum and cross-spectrum analysis (Figures 12 through 15). The autospectrum functions $S(+l, \omega)$ and $[S(-l, \omega)]$ represent poleward propagating and equatorward propagating variance density, respectively, and they are computed over grid points 4 through 13 using the two-dimensional Fourier transform method as outlined by *Halliwell and Allen* [1987]. The Nyquist wave number is 2.78×10^{-3} cycles per kilometer (cpkm), but all spectrum functions are presented only for $-2.2 \times 10^{-3} \leqq l \leqq 2.2 \times 10^{-3}$ cpkm since calculated winds poorly represent fluctuations at larger l, and since measured winds may also not represent fluctuations well because the alongshore spacing between some measurement stations is > 180 km.

The variance density in (l, ω) space for calculated, adjusted measured, and measured winds decreases with increasing l and ω for all three seasons (Figure 12). The decrease with increasing l is more rapid for calculated than adjusted measured winds, resulting from the poor representation of smaller-scale fluctuations by calculated winds. The variance density distributions of all wind sets are similar in each season at $l \leqq 1.1 \times 10^{-3}$ cpkm (wavelengths $\geqq 900$ km). (We select this particular value of l as the boundary between the energetic large

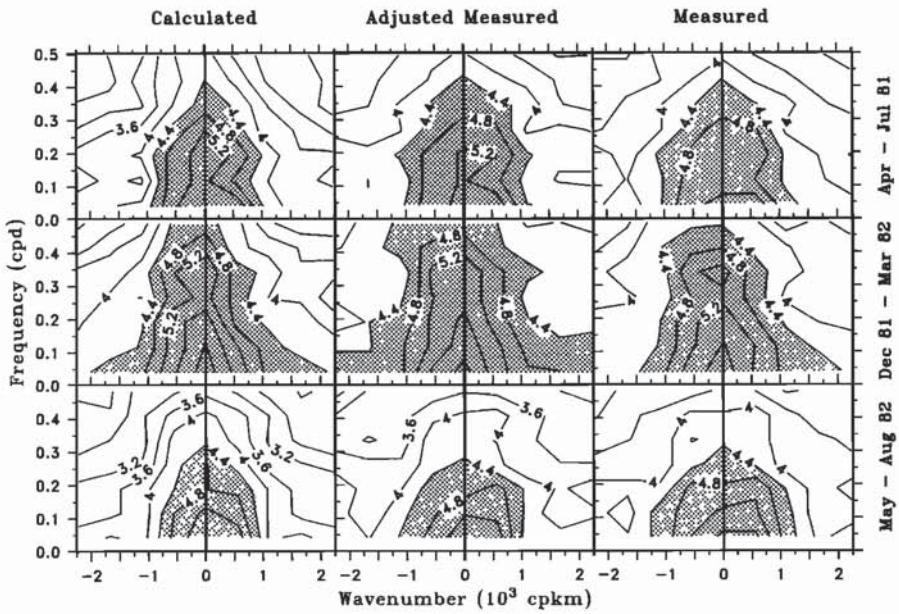

Fig. 12. Wave number–frequency autospectra of calculated, adjusted measured, and measured alongshore winds over grid points 4 through 13 for the three seasons. The contours are of $\log_{10}[S(\pm l, \omega)]$, with S in units of $m^2\ s^{-2}\ cpd^{-1}\ cpkm^{-1}$. The autospectra have been band-averaged over nine frequency bands only, so the resulting number of degrees of freedom is 18 [*Halliwell and Allen*, 1987]. The 95% confidence limits are between $\log_{10} S - 0.24$ and $\log_{10} S + 0.34$ at all l and ω. The autospectra are shaded where $S(\pm l, \omega) > 10^{4.4}$. The wave numbers and frequencies at which spectrum estimates exist are shown in Figure 14.

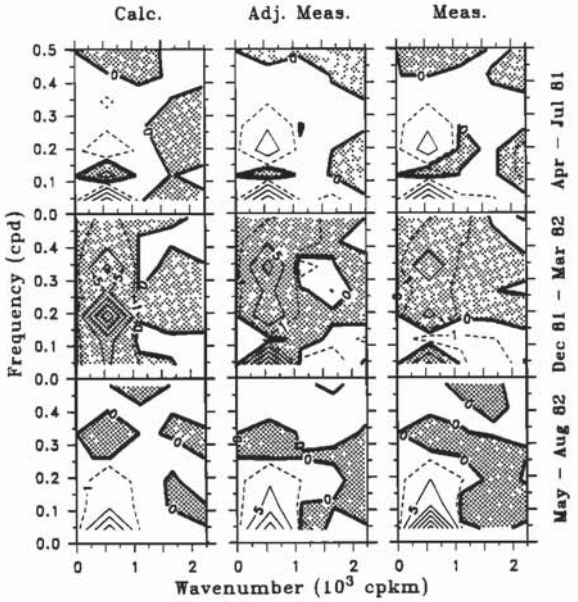

Fig. 13. Wave number–frequency propagating autospectra of calculated adjusted measured, and measured alongshore winds over grid points 4 through 13 for the three seasons. The contours are of $10^{-4}[S(+l, \omega) - S(-l, \omega)]$, with S in units of $m^2\ s^{-2}\ cpd^{-1}\ cpkm^{-1}$. The number of degrees of freedom is 18. Negative (equatorward propagating) autospectra are shaded. The wave numbers and frequencies at which spectrum estimates exist are shown in Figure 14.

scales and the much less energetic small scales because it is one at which spectrum estimates are computed; see Figure 14.) From the results of a statistical F test similar to that performed in section 4.1, significant differences between calculated and adjusted measured wind spectrum estimates exist only in those parts of (l, ω) space where the calculated wind autospectra are roughly within the following ranges: $\log_{10}S < 3.6$ during summer 1981, $\log_{10}S < 4$ during winter 1981–1982, and $\log_{10}S < 3.2$ during summer 1982. Therefore these distributions of calculated wind variance density in (l, ω) space for the three seasons are not significantly different from those of adjusted measured wind, except at the largest l and ω (roughly $l \geqq 1.2 \times 10^{-3}$ cpkm and $\omega \geqq 0.3$ cpd) where very little wind variance exists. This is true despite the large variability along the coast in measured alongshore wind variance (Figure 8). The (l, ω) autospectra indicate that the distribution of variance density in the wave number domain is also not changed significantly by adjusting the measured wind variance. Apparently the function $\xi_{s,m}(y)$ in (5) has the property that it does not significantly alter the distribution of the variance of $v_a(y, t)$ in (l, ω) space from that of $v_m(y, t)$.

The basic patterns in the contours of propagating autospectra of calculated, adjusted measured, and measured winds (Figure 13) are similar to each other in all seasons. Equatorward propagating variance exceeds poleward in winter, with the greatest excess at $l \leqq 1.1 \times 10^{-3}$ cpkm. In the two summers, poleward propagating variance generally exceeds equatorward for $l \leqq 1.1 \times 10^{-3}$ cpkm and $\omega \leqq 0.41$ cpd (excluding 0.11 cpd) in summer 1981 and $\omega < 0.26$ cpd in summer 1982.

The spectral shapes in the l and ω domains are illustrated by integrating the (l, ω) autospectra over ω and l, respectively (Figure 14). From the l autospectra, the dominance of wind fluctuations with $l \leqq 1.1 \times 10^{-3}$ cpkm is evident in all three winds sets for all three seasons. Over 90% of calculated wind variance and about 80% of adjusted measured wind variance is due to fluctuations with $l \leqq 1.1 \times 10^{-3}$ cpkm in all seasons (Table 5). Adjusting or normalizing the wind fields only slightly decreases these percentages. The spectral shapes for both measured and adjusted measured winds are very similar (Figure 14). There is little difference in the percentage of total variance with $l \leqq 1.1 \times 10^{-3}$ cpkm among the three seasons (Table 5), but relatively more variance is observed at $l = 0$ (essentially representing wavelengths of >2000 km) during winter 1981–1982 than during the two summers. The distributions in l space are skewed toward equatorward propagation (larger variance density for $-l$) in winter and toward poleward propagation in the two summers.

The integrated ω autospectra have similar spectral shapes for all three seasons (Figure 14). They decrease monotonically with increasing ω, with two exceptions: In summer 1981, a relative minimum exists near 0.11 cpd and a relative maximum exists near 0.19 cpd. In winter 1981–1982 a relative minimum exists near 0.26 cpd and a relative maximum exists near 0.34 cpd. These extrema are all evident in the (y, ω) autospectra of alongshore wind (Figure 8). The variance density decreases by 2 orders of magnitude over the entire frequency band ($0.04 \leqq \omega \leqq 0.48$ cpd) in summer 1982, and it decreases by 1 order of magnitude in the other seasons, with the smallest decrease occurring in winter 1981–1982. Summer 1981 variance density exceeds that in summer 1982 for $\omega > 0.11$ cpd.

Squared coherences between calculated winds and both adjusted measured and measured winds (Figure 15) are large only for $l \leqq 1.1 \times 10^{-3}$ cpkm in all seasons. The variation of coherence with l, ω, and season tends to follow that of wind variance density, with high coherence generally found where the variance density is relatively large. The coherence decays more rapidly with increasing ω in the two summers than in winter, which is probably related to the relatively large winter variance density at higher frequencies. In winter, coherence is larger for equatorward propagating variance than for poleward propagating variance. In summer there is a slight tendency for the poleward propagating variance to be more coherent. It is again remarkable to observe the strong similarity of coherence patterns (Figure 15) between calculated winds and both adjusted measured and measured winds despite the large alongshore variability in measured alongshore wind variance. The coherence decays slightly more rapidly with increasing $|l|$ for measured winds than for adjusted measured winds in all seasons. Alongshore errors in wind variance therefore have very little effect on (l, ω) spectrum analyses.

5. Characteristics of Wind Fluctuation Events

5.1. *Space-Time Contour Plots of Alongshore Wind*

We use space-time contour plots of alongshore wind to visually characterize the basic properties of alongshore winds and to illustrate how these properties change among seasons, with alongshore location, and with time within a given season. We compare the representation of wind events by the calculated and measured wind sets, and we utilize National Weather Service surface atmospheric pressure charts to establish the basic relationships of surface synoptic-scale atmospheric pressure systems to observed wind event properties.

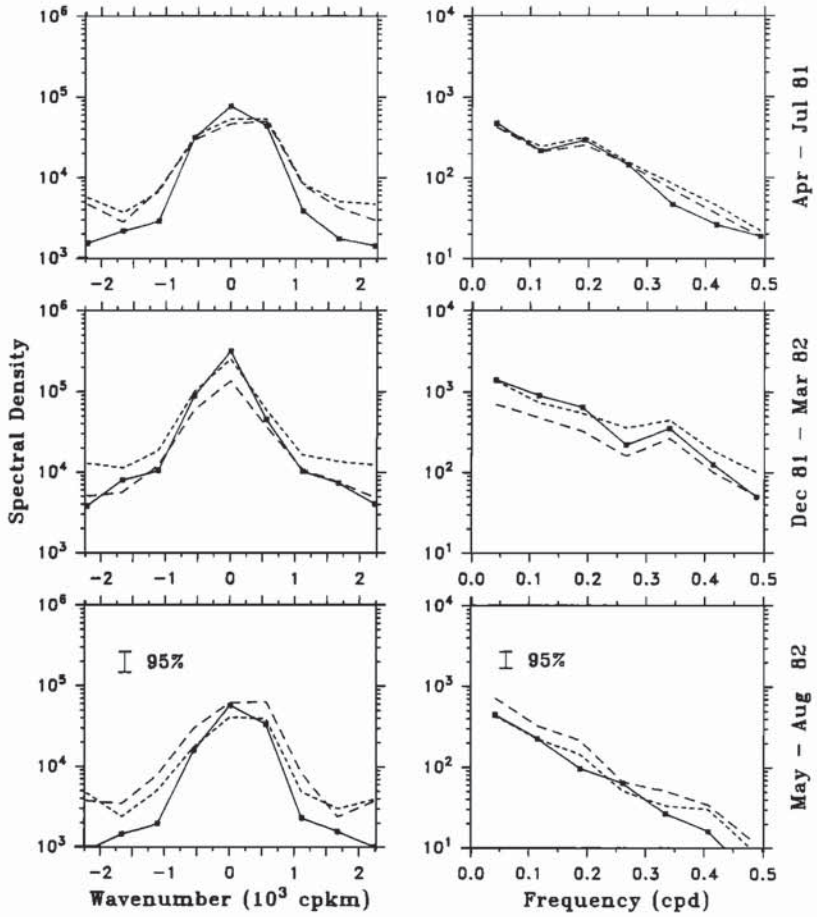

Fig. 14. (left) Integrated wave number autospectra and (right) integrated frequency autospectra for calculated (solid), adjusted measured (short-dashed lines), and measured (long-dashed lines) alongshore winds over grid points 4 through 13 for the three seasons. The integrated wave number (frequency) autospectra are computed with 126 (198) degrees of freedom; 95% confidence bands are shown.

To illustrate typical characteristics of alongshore wind fluctuations they are contoured for three 45-day subintervals, one from each of the 4-month seasons, for calculated winds, adjusted measured winds, and measured winds (Figures 16 through 18). We refer to extrema of equatorward (poleward) wind as upwelling (downwelling) events. The variance adjustment of the measured winds usually enhances the amplitudes of wind extrema poleward of the Oregon-California border ($y < 400$ km). Adjusted measured winds are visually correlated with calculated winds, and this visual correlation is substantially enhanced by removing the mean wind prior to contouring (not shown), especially in summer.

Substantial differences in wind event properties exist between winter and summer. During the winter subinterval, strong wind events of 2 to 4 days duration dominate the fluctuations, most of which either are in phase along the coast or tend to propagate equatorward (Figure 17). Some of these winter events affect the entire CODE large-scale domain. During the two summer subintervals, strong equatorward mean winds exist along the California coast ($-1000 < y <$ 400 km) and wind events are typically confined within 1000 to 1500 km alongshore subdomains (Figures 16 and 18). This seasonal difference in the alongshore scales of wind fluctuations is also found in the alongshore correlation space scales (Table 4), the alongshore coherence scales (Figure 11), and the integrated wave number autospectra (Figure 14, where a larger percentage of total variance in winter is due to fluctuations with alongshore wavelengths >2000 km). A preferred propagation direction for wind fluctuations is not visually evident in summer, although (l, ω) autospectra indicate that the preferred direction is poleward, especially at low frequency (Figure 13).

5.2. *Winter Event Properties*

During the winter subinterval (Figure 17), equatorward propagating alongshore wind fluctuations occur between February 15 and 27, 1982. A downwelling event occurs essentially in phase along the coast throughout the entire CODE large-scale domain on March 1. Poleward propagating wind fluctuations occur from March 3 to 9, followed by equatorward propagating fluctuations from March 10 to 18. Smaller-amplitude, lower-frequency fluctuations exist after March 18, which tend to occur in phase or propagate equatorward. The interval from March 3 to 9 is the longest one in winter 1981–1982 where poleward propagation dominates. In-phase or equatorward propagating fluctuations dominate during most of that winter.

Propagating surface synoptic-scale pressure systems are responsible for these observed properties. For example, the in-phase downwelling event of March 1, 1982, is caused by a

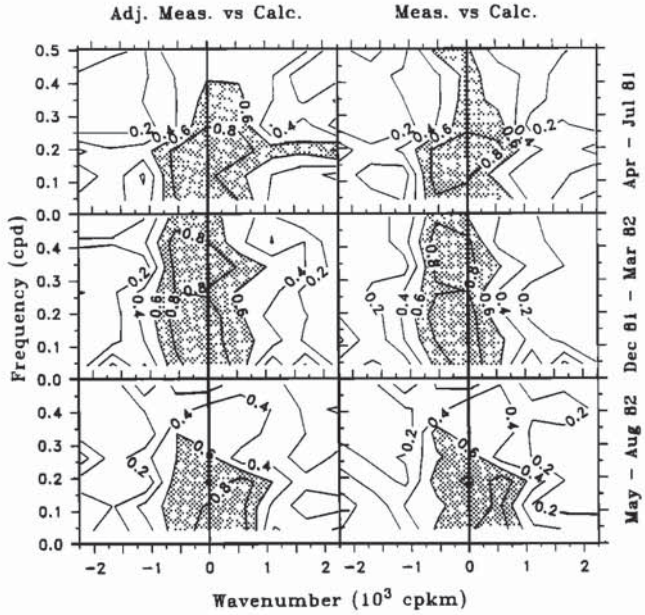

Fig. 15. Wave number–frequency squared coherences between adjusted measured and calculated alongshore winds and between measured and calculated alongshore winds over grid points 4 through 13 for the three seasons. Squared coherences greater than 0.6 are shaded. Squared coherences greater than 0.16 are significant to a 95% level of confidence. The wave numbers and frequencies at which coherence estimates exist are shown in Figure 14.

large cyclone that moves directly onshore near Vancouver Island ($1110 < y < 1470$ km) and has closed pressure contours that affect the entire large-scale domain poleward of Baja California ($y > -1000$ km). (When we refer to a cyclone, we include the fronts associated with it.) The winds become poleward almost simultaneously in the entire coastal region affected by the cyclone as it approaches the coast with its anticlockwise wind circulation. The wind then subsides along the coast as the cyclone both moves inland and weakens rapidly. The event persists for an extra day along the coast between northern California and southern British Columbia ($200 < y < 1400$ km) (Figure 17). Between March 3 and 9, atmospheric cyclones and anticyclones propagate from southwest to northeast, first affecting the southern and central California coast, then the Oregon, Washington, and British Columbia coasts. Between March 10 and 18 a series of cold fronts and anticyclones propagate from northwest to southeast from the Gulf of Alaska across the northwest U.S. coast. These systems become weaker and occur less frequently after March 18. Over time scales of the order of several days, the properties of winter propagating synoptic-scale systems can differ substantially from seasonal mean properties.

A typical example of the equatorward alongshore progression of winter weather systems is shown for the interval March 11 to 14 (Figure 19). Two cold fronts, separated by an anticyclone, propagate rapidly from northwest to southeast during this time interval, and two equatorward propagating pulses of strong equatorward winds follow the frontal passages (Figure 17). These winter cold fronts trailing to the south or southwest from the cyclone centers usually propagate toward the east or southeast, giving the propagation an equatorward alongshore component, even when the parent cyclone propagates to the north of due east. Southeastward propagating fronts are common in winter and probably produce the preference for equatorward propagation in the winter wind field. *Halliwell and Allen* [1987] show that equatorward propagation dominates in all four winters from 1980–1981 to 1983–1984.

5.3. *Summer Event Properties*

In the two summer subintervals (Figures 16 and 18), some individual wind events have a preferred propagation direction, but preferred directions usually do not persist over several-day intervals as is often observed during winter. Cyclones often generate strong downwelling events in the northern part of the CODE large-scale domain during the summer subintervals. These events are usually separated by 2 to 6 days in both the summer 1981 subinterval (Figure 16) and the first half of the summer 1982 subinterval (Figure 18) and affect the coast farther to the south on average during summer 1981. In particular, downwelling events penetrate equatorward to the CODE site on May 18 and June 8 to 9, 1981. Upwelling events along the U.S. coast ($-1000 < y < 1100$ km) often occur 2 to 4 days after the passage of these cyclones (Figures 16 and 18), and they are usually strongest along the California coast ($-1000 < y < 400$ km), excluding the Southern California Bight ($-1000 < y < -550$ km) for measured winds. These upwelling events also tend to be centered farther to the south in summer 1981 than in summer 1982.

During the summer 1981 subinterval, the strongest upwelling events occur on May 30 to 31, June 9 to 11, June 13 to 15, and June 26 to 28. Based on surface weather charts, all four of these events follow the passage of cyclones in the northern half of the CODE large-scale domain, although the cyclones that precede the last two events weaken very rapidly as they reach the coast and do not produce strong downwelling events (Figure 16). The cyclone preceding the June 13 to 15 upwelling event causes poleward alongshore winds on June 12 to 13 primarily along the Oregon coast only (centered near $y = 600$ km), and the cyclone preceding the June 26 to 28 upwelling event causes poleward alongshore winds on June 24 to 25 along the extreme northern British Columbia coast ($y > 1400$ km) in the calculated wind field only. In the event cycle from May 28 to 31 (Figure 20), a cyclone approaches the British Columbia coast on May 28 and 29, and the trailing cold front has passed the coast southward to northern California by May 30. The North Pacific subtropical high has intensified northeastward toward the U.S. coast by May 31, increasing the pressure gradient and coastal wind speed between the high and the thermal low over the southwest U.S. The pressure gradient at the California coast south of Cape Mendocino (40°N) is about twice as strong on May 31 as on May 28, and

TABLE 5. Percentage of Total Variance Due to Alongshore Wind Fluctuations With Wavelengths of ≥900 km Determined From Wave Number–Frequency Autospectra Integrated Over Frequency (Figure 14)

Wind Set	Time Interval		
	April–July 1981	Dec. 1981–March 1982	May–Aug. 1982
Calculated	93	92	94
Normalized calculated	91	91	89
Measured	83	85	85
Adjusted measured	80	82	79
Normalized measured	80	81	80

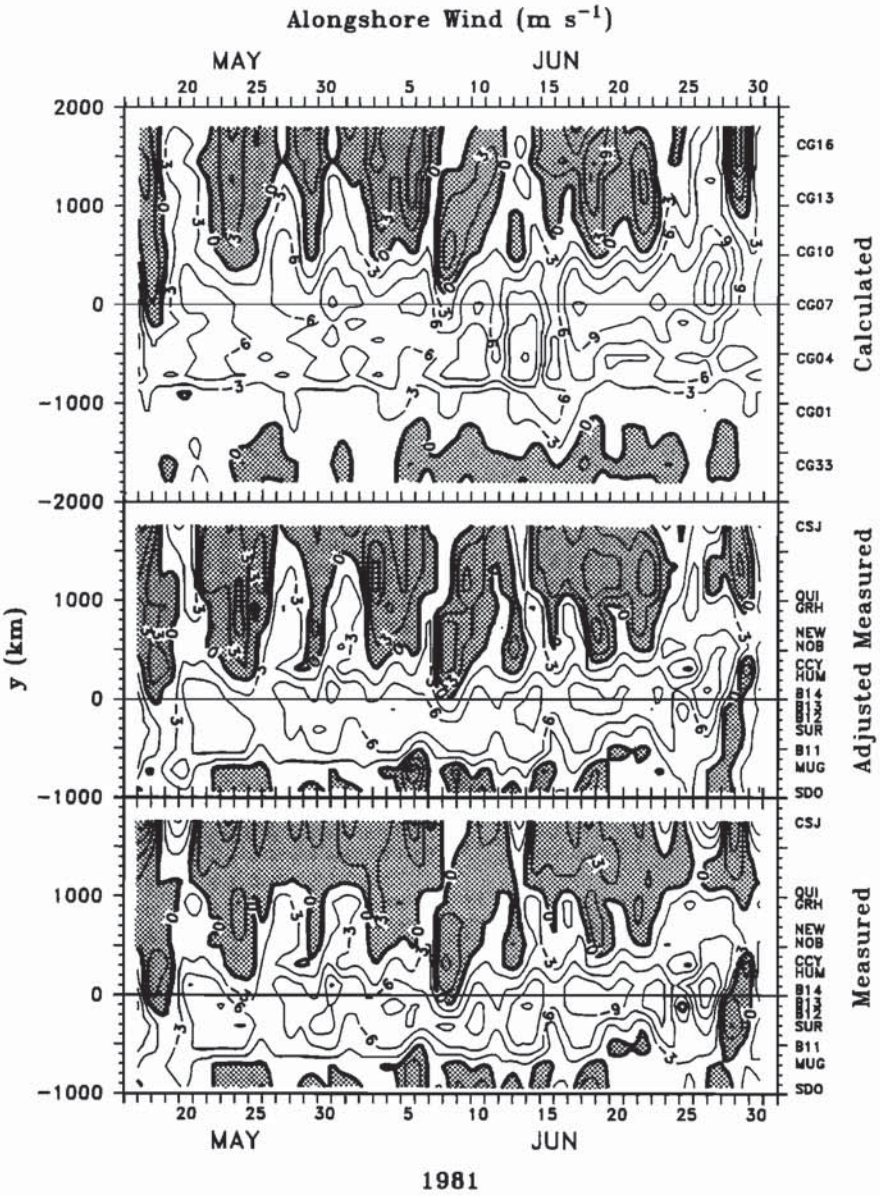

Fig. 16. Calculated, adjusted measured, and measured alongshore wind contoured as a function of time and y for May 17 through June 30, 1981. The contour interval is 3 m s^{-1}. Positive (poleward) wind is shaded. The prefix "CG" on the grid point numbers signifies "CODE grid".

the measured alongshore wind speed near the CODE site (Figure 16) has also about doubled.

During the summer 1982 subinterval, the strongest upwelling events occur on May 3 to 4, May 8 to 9, May 17 to 18, May 22 to 23, and May 26 to 27, 1982, and they all follow cyclones that induce strong downwelling events (Figure 18). These event cycles are similar to those observed in summer 1981, except for being shifted to the north on average. In the event cycle from May 15 to 18 (Figure 21), the cyclone strikes the British Columbia coast on May 16, and the associated cold front passes the northwest U.S. coast by May 17. During the 2 days after frontal passage, the subtropical high intensifies northeastward, producing strong equatorward winds. The coastal pressure gradient near the CODE site on May 18, 1982, is about 40% stronger than it was 3 days earlier (Figure 21), which is about the percentage increase of measured alongshore wind speed near the CODE site. *Mass et al.* [1986] study similar summer event cycles in great detail, emphasizing how they drive onshore surges of cool marine air along the northwest U.S. and Canadian coasts. They show that as the cyclones and associated fronts approach the coast, coastally trapped pressure systems are generated which drive coastal gravity currents that enhance the poleward alongshore wind in the northern part of the large-scale domain caused by the synoptic-scale systems.

Downwelling events centered along the California coast occasionally follow these upwelling events in both summers. These downwelling events are clearly represented in the measured wind contour plots but are poorly represented in the calculated wind contour plots (Figures 16 and 18). The strongest of these events during the two summer subintervals occur on June 28 to 30, 1981; May 4 to 6, 1982; and May 24

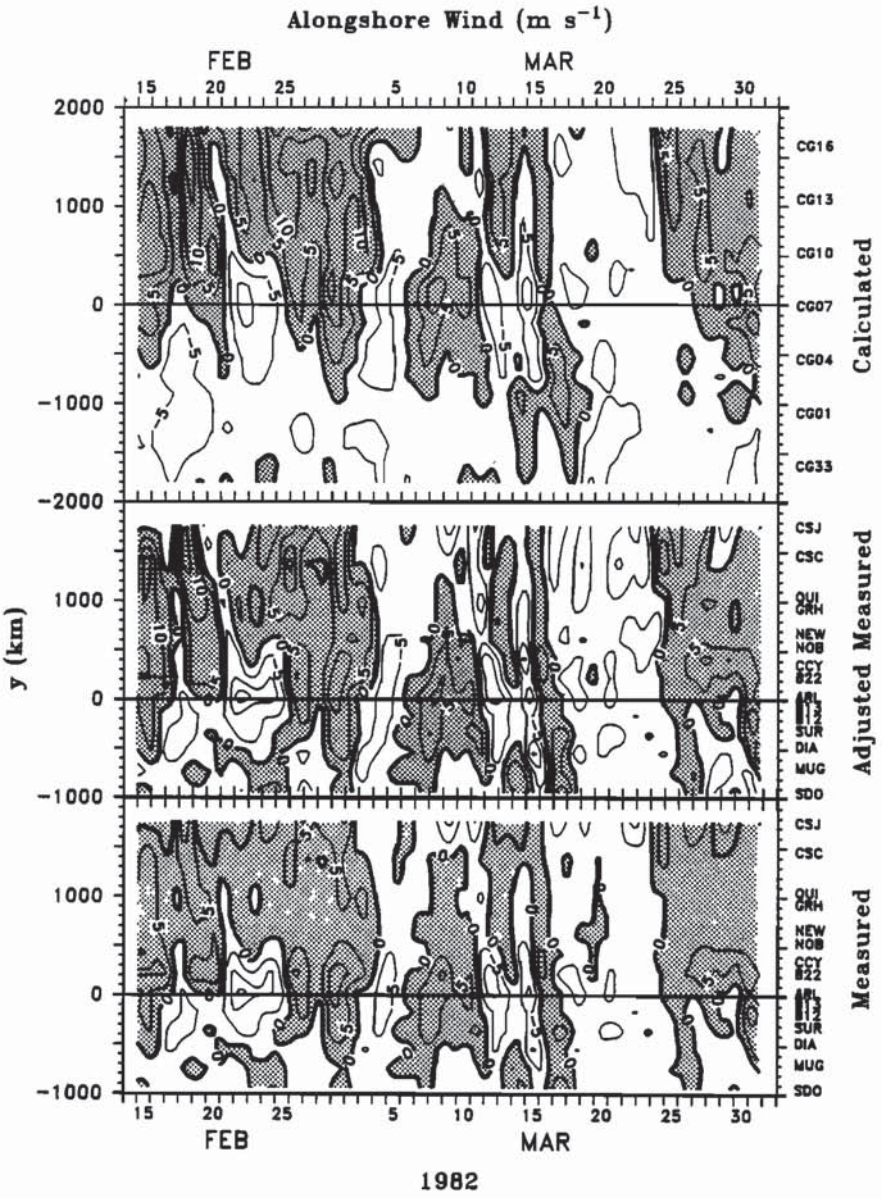

Fig. 17. As in Figure 16, except for February 15 through March 31, 1982. The contour interval here is 5 m s^{-1}.

to 26, 1982. These events are evidently associated with coastally trapped atmospheric pressure disturbances [*Dorman*, 1985, this issue]. Since the atmospheric internal Rossby radius of deformation is about 150 km along the California coast, these disturbances have an across-shore scale substantially smaller than the alongshore scale, probably causing the calculated winds to poorly resolve them. To crudely determine how well the calculated wind field reproduces the event of May 4 to 6, we compare the maximum changes in calculated and measured alongshore wind speeds caused by the event at both grid point 6 and station B12 (near $y = -180$ km), the approximate location of the largest speed change. The measured alongshore wind changes from -10 to $+6$ m s^{-1} between May 3 and 5, while the calculated wind changes from -9 to -2 m s^{-1}, or only 44% of the measured wind change.

During the last third of the summer 1982 subinterval (following about May 28), calculated alongshore wind fluctuations are relatively small, and event cycles such as the ones we have discussed for both 1981 and 1982 are not evident (Figure 18). This relatively quiet pattern dominates most of the remainder of the 4-month summer 1982 season, and a similar quiet period occurs after July 10 in the 4-month summer 1981 season. Quiet intervals dominate about 20% of summer 1981 and nearly two thirds of summer 1982. No propagating cyclones or associated fronts are evident in the surface pressure field during a typical quiet interval (May 28 to 31, 1982; Figure 22). The subtropical high extends much farther to the north during this interval, and cyclones remain far to the north of the CODE large-scale domain. Although propagating systems are not evident at the surface, the pressure field does not remain steady between May 28 and 31 (Figure 22) because the subtropical high weakens and the thermal low builds northward to cover nearly the entire western United States over this 4-day interval. During intervals when propagating systems are very weak or absent, oscillations in the relative strengths and positions of the subtropical high and

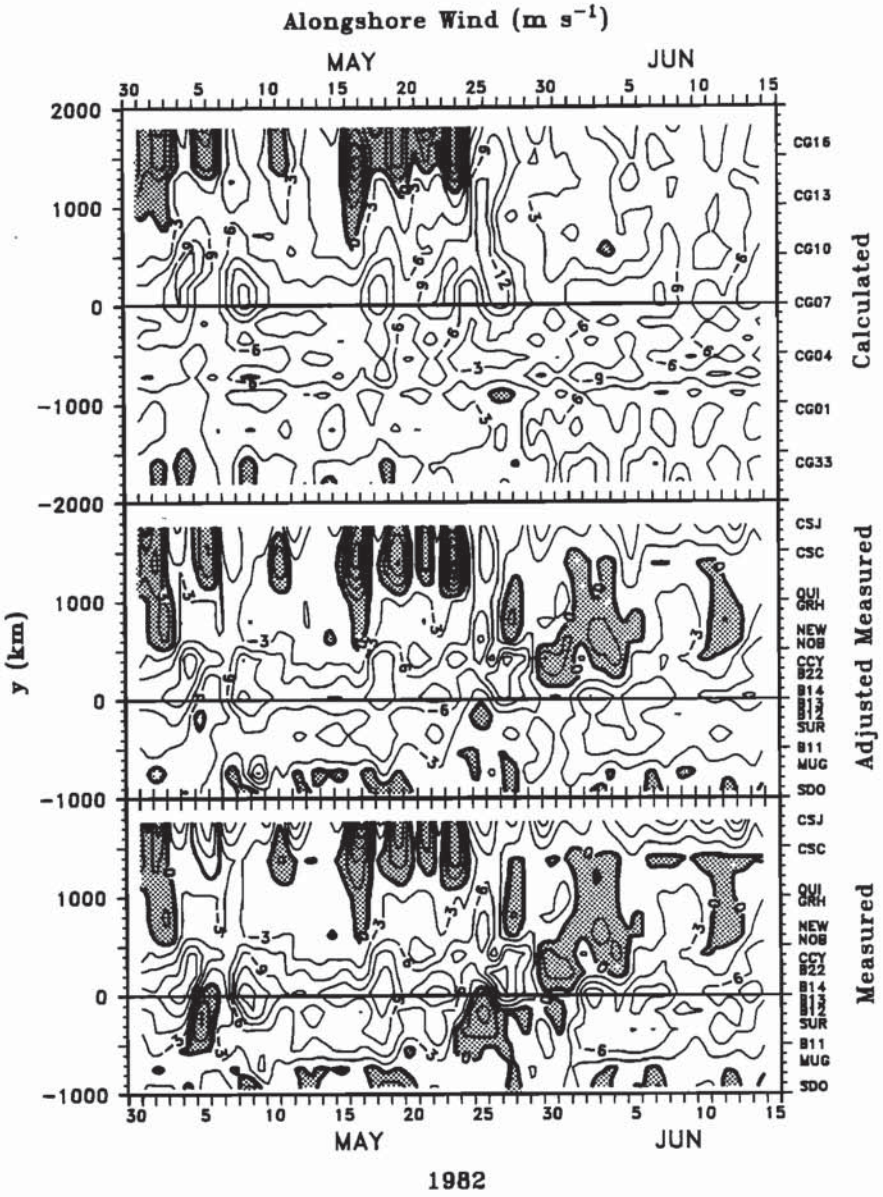

Fig. 18. As in Figure 16, except for May 1 through June 14, 1982.

thermal low may still have an important influence on coastal surface winds.

Measured alongshore wind fluctuations are substantially larger than those for calculated alongshore wind during these quiet intervals (Figure 18), which may be partly caused by coastal boundary layer processes. For example, propagating atmospheric systems (troughs and ridges) that have a very weak pressure signal at the surface still exist in the middle troposphere during these quiet intervals. Passage of these systems can raise or lower the marine inversion layer, indirectly affecting coastal winds [*Beardsley et al.*, this issue]. Strong equatorward measured winds exist near the latitudes of the CODE site between June 1 and 8, 1982, but this event is not as evident in the calculated wind field (Figure 18). During this interval, enhanced northwest winds to the west of a pressure trough at the 700-mbar level (height ≈ 3 km) in the atmosphere change the across-shore structure of the marine inversion layer by raising it near the coast, making the actual equatorward alongshore winds at the coast stronger than could be accounted for by the synoptic-scale pressure gradient alone [*Beardsley et al.*, this issue].

We can visually assess the characteristics of the summer measured alongshore winds within the Southern California Bight ($-1000 < y < -550$ km) and see how they differ from the calculated winds there by inspecting wind events (Figures 16 and 18). Several time intervals can readily be identified where measured alongshore wind in the bight opposes the measured alongshore wind poleward of the bight. These include most of the interval from June 5 to 13, 1981; May 5 and 6, 1982; May 17 to 20, 1982; and most of the interval from June 2 to 7, 1982. In contrast, the calculated alongshore wind in the bight does not oppose the calculated alongshore wind poleward of the bight during these time intervals. From surface weather charts, wind patterns within the bight resemble cyclonic Catalina eddy events [*Bosart*, 1983] during the June 5 to 13, 1981, and May 17 to 20, 1982, intervals.

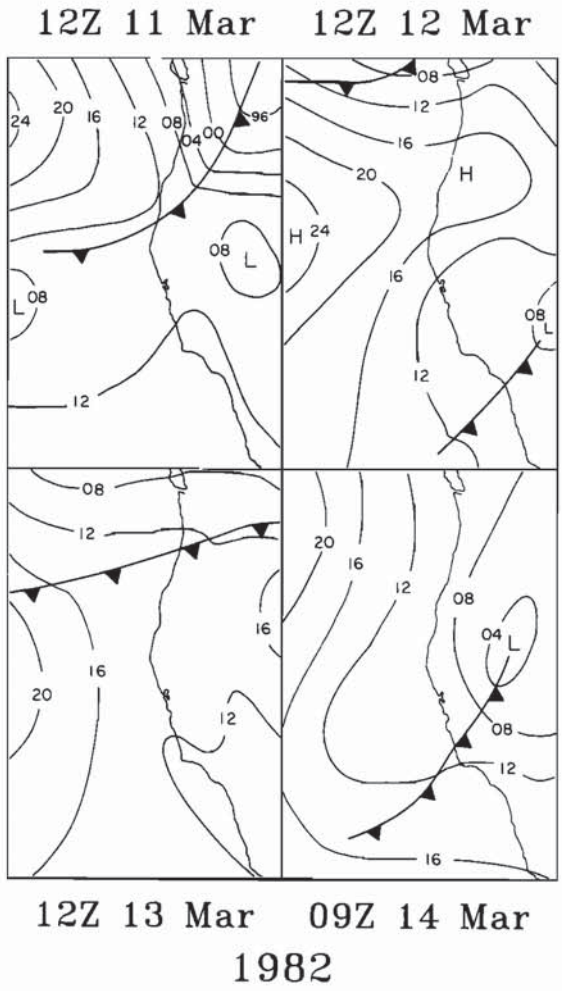

Fig. 19. Surface atmospheric pressure charts for March 11 to 14, 1982 (from National Weather Service surface meteorological charts).

6. Discussion

The properties of coastal wind fluctuations along the west coast of North America vary over a wide range of time scales. The wind properties have a large seasonal cycle due to changes in the properties of both synoptic-scale pressure systems and the coastal marine boundary layer. Winter winds are primarily driven by propagating cyclones and anticyclones, so the statistical properties of wind fluctuations depend strongly on the size, strength, propagation speed and direction, and frequency of occurrence of these systems. These properties often remain relatively constant for several days and then change abruptly. The summer situation is more complicated owing to the continuous existence of a strong inversion layer in the coastal marine boundary and to the existence of two permanent pressure systems: the North Pacific subtropical high and the southwest U.S. thermal low. The interaction between propagating surface cyclones, which are weaker on average than in winter, and these stationary systems has an important influence on summer winds. In particular, the subtropical high often builds northeastward toward the coast after a cyclone passes to the north of the high, causing strong upwelling events along the California coast. The high occasionally builds far to the north for days to weeks at a time, keeping propagating cyclones far to the north of the CODE large-scale domain. During these intervals, oscillations in the strength and position of the subtropical high and thermal low, plus coastal boundary layer processes, have an important influence on coastal winds. Coastally trapped atmospheric disturbances can enhance downwelling events ahead of cyclones approaching the coast and cause relaxations or reversals in the mean equatorward wind along the California coast.

These properties of atmospheric systems and the coastal marine boundary layer lead to the following seasonal similarities and differences in measured wind statistics along the west coast of North America: Mean summer winds have an equatorward alongshore component throughout the domain, except at the northern end during summer 1981, and are relatively strong along the California coast. The largest mean exists near the CODE experimental site northwest of San Francisco. Mean winter winds have a poleward component north of the CODE site and an equatorward component to the south. Wind fluctuations are strongly polarized in the alongshore direction in all seasons but are less so in winter. Wind fluctuations are relatively large near the CODE site in summer, near Cape Mendocino in winter, and at the northern end of the large-scale domain (northern British Columbia) in both seasons. Winter fluctuations have larger amplitudes and larger space scales than in summer. They have a strong tendency to propagate equatorward at all frequencies, while summer fluctuations have a tendency to propagate poleward.

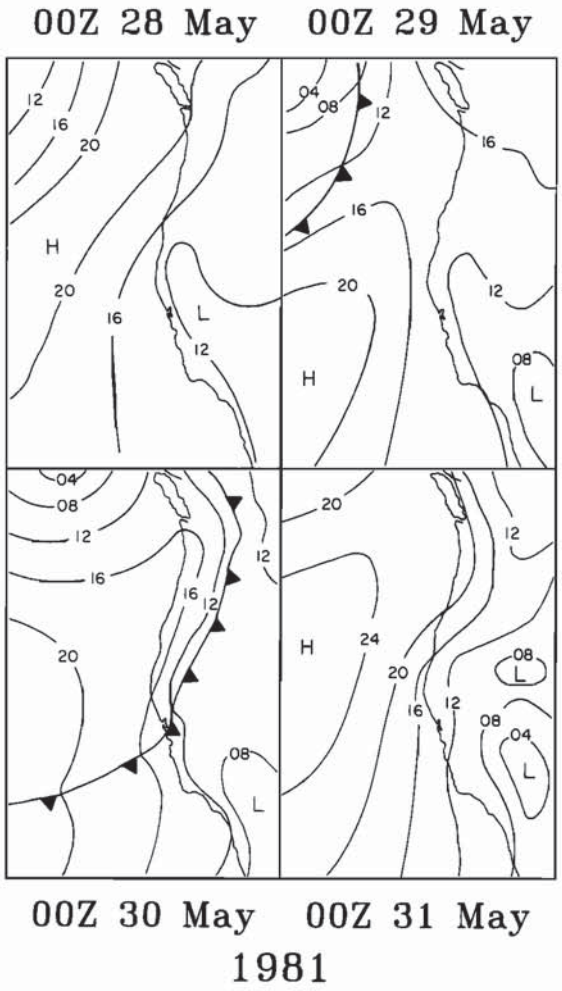

Fig. 20. As in Figure 19, except for May 28 to 31, 1981.

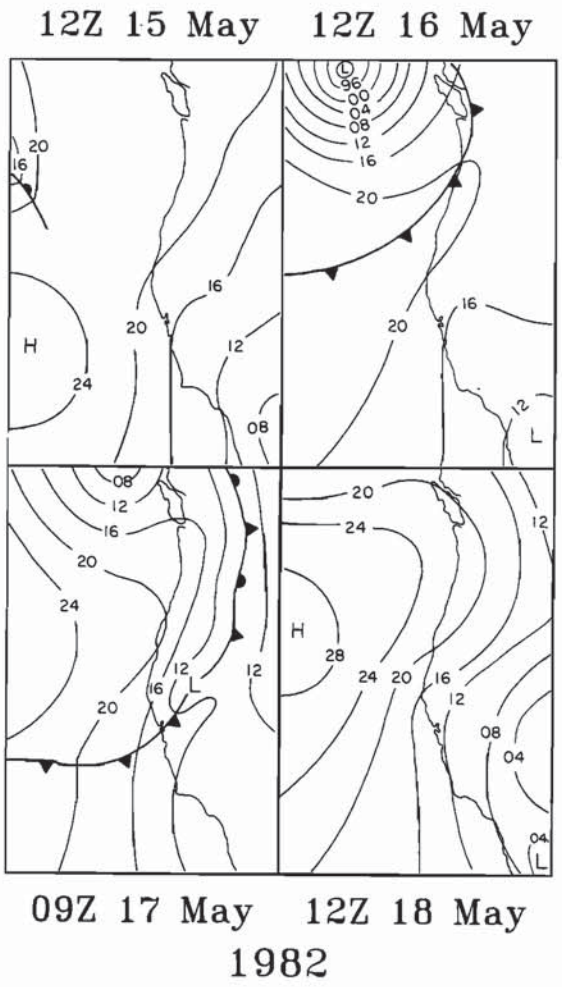

Fig. 21. As in Figure 19, except for May 15 to 18, 1982.

In summer, poleward propagating coastally trapped pressure disturbances may contribute to the directional preference. In all seasons, about 80% to 85% of measured wind variance is due to fluctuations with wavelengths greater than 900 km. Coastal atmospheric boundary layer processes appear to primarily influence the variance of measured alongshore wind without seriously affecting other statistical properties.

Wind variance is larger, and wind autospectra are less red, in summer 1981 than summer 1982. The subtropical high extends far to the north, preventing propagating cyclones from affecting the large-scale domain at all, for nearly two thirds of summer 1982. This pattern exists for only about 20% of summer 1981. Winds tend to fluctuate at lower frequency and have smaller amplitudes under these conditions, which probably accounts for much of the observed differences in wind statistics between the two summers. *Denbo and Allen* [this issue] report substantial differences in wind stress properties in two 64-day intervals in summer 1981 (May 8 to July 11) and summer 1982 (May 26 to July 29). From the study of surface pressure charts here, we find that the influence of propagating cyclones and anticyclones is much weaker during most of their summer 1982 interval than during their summer 1981 interval, and this is presumably a major cause of the observed differences in wind stress properties.

The statistical properties of wind fluctuations therefore differ substantially between winter and summer and between different years for the same season. Within a given season, properties such as the fluctuation amplitude, the frequency of the fluctuations, and the propagation direction can be relatively constant over time intervals of several days to several weeks. These intervals are separated from one another by abrupt changes in some or all of these properties. Studies of the response of coastal currents to wind forcing during one season, or a small subset of one season, may not represent typical conditions for that season.

The calculated and measured alongshore wind sets are very coherent for wavelengths of $\geqq 900$ km throughout the large-scale domain, except within the Southern California Bight in summer. Calculated alongshore winds poorly represent fluctuations with wavelengths of <900 km. They represent fluctuations caused by coastal boundary layer processes, but with less than half the amplitude of the measured winds. Outside of the bight, the primary difference between the two alongshore wind sets for wavelengths of $\geqq 900$ km is in the representation of wind variance as a function of alongshore location. For example, a large maximum in measured alongshore wind variance exists along the northern California coast in both summer and winter, which does not exist in the calculated alongshore winds. However, we found that many statistical analyses are not sensitive to errors in the distribution of wind variance along the coast. We conclude that poleward of the Southern California Bight in summer and everywhere along

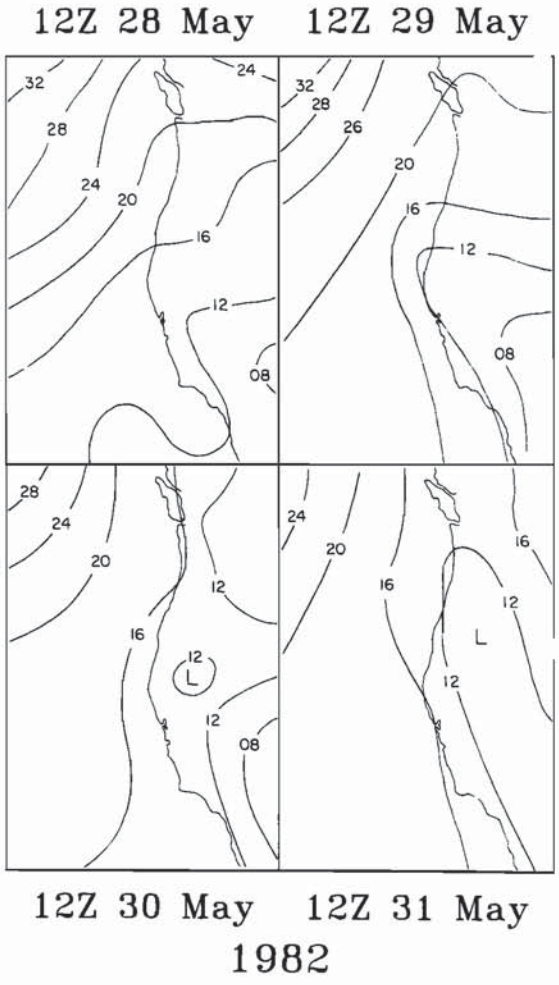

Fig. 22. As in Figure 19, except for May 28 to 31, 1982.

the coast in winter, both wind sets should perform reasonably well as forcing functions for wavelengths of $\geqq 900$ km and $\omega < 0.5$ cpd in studying properties of the coastal ocean response that do not depend on the absolute magnitude of wind variance.

APPENDIX

We estimate the magnitude of the minimum correlation coefficient that is significantly different from zero using the number of degrees of freedom based on the independence time scale discussed by *Davis* [1976]. These time scales vary with alongshore location and season, but for those stations with the largest time scales, the number of degrees of freedom is about 35, resulting in a "worst-case" estimate of 0.35 for the minimum significant correlation at the 95% level of confidence. We therefore use this value as the minimum significant correlation for all time series.

Acknowledgments. This research was performed with the support of the Oceanography section of the National Science Foundation under grants OCE-8014939 and OCE-8411613 as part of the Coastal Ocean Dynamics Experiment (CODE). We thank D. B. Enfield, S. Esbensen, and K. H. Brink for helpful comments on a draft manuscript. We express our gratitude to the organizations and people that have provided the wind data used in this study. We especially thank Andrew Bakun for help in obtaining the calculated wind set. Figures 1 to 18 were generated using the interactive graphics package PLOT5 developed by Donald W. Denbo. CODE contribution 38.

REFERENCES

Bakun, A., Daily and weekly upwelling indices, west coast of North America, 1967-73, *NOAA Tech. Rep. NMFS SSRF-693*, 114 pp., 1975.

Beardsley, R. C., C. E. Dorman, C. A. Friehe, L. K. Rosenfeld, and C. D. Winant, Local atmospheric forcing during the Coastal Ocean Dynamics Experiment, 1, A description of the marine boundary layer and atmospheric conditions over a northern California upwelling region, *J. Geophys. Res.*, this issue.

Bosart, L. F., Analysis of a California Catalina eddy event, *Mon. Weather Rev.*, *111*, 1619–1633, 1983.

Brink, K. H., D. W. Stuart, and J. C. Van Leer, Observations of the coastal upwelling region near 34°30'N off California: Spring 1981, *J. Phys. Oceanogr.*, *14*, 378–391, 1984.

Clarke, A. J., Observational and numerical evidence for wind-forced coastal trapped long waves, *J. Phys. Oceanogr.*, *7*, 231–247, 1977.

Davis, R. E., Predictability of sea surface temperature and sea level pressure anomalies over the North Pacific Ocean, *J. Phys. Oceanogr.*, *6*, 249–266, 1976.

Denbo, D. W., and J. S. Allen, Large-scale response to atmospheric forcing of shelf currents and coastal sea level off California and Oregon: May–July 1981 and 1982, *J. Geophys. Res.*, this issue.

Dorman, C. E., Evidence of Kelvin waves in California's marine layer and related eddy generation, *Mon. Weather Rev.*, *113*, 827–839, 1985.

Dorman, C. E., Possible role of gravity currents in northern California's coastal summer wind reversals, *J. Geophys. Res.*, this issue.

Friehe, C. A., and C. D. Winant, Observations of wind and sea surface temperature structure off the northern California coast, paper presented at the First International Conference on Meteorology and Air-Sea Interaction of the Coastal Zone, The Hague, Netherlands, May 10–14, 1982.

Friehe, C. A., and C. D. Winant, Contoured aircraft survey data for CODE-1, 1981, *SIO Ref. Ser*, *84-20*, Scripps Inst. of Oceanogr., Univ. of Calif., La Jolla, 1984.

Gill, A. E., and E. H. Schumann, The generation of long shelf waves by the wind, *J. Phys. Oceanogr.*, *4*, 83–90, 1974.

Gonella, J., A rotary component method for analyzing meteorological and oceanographic time series, *Deep Sea Res.*, *19*, 833–846, 1972.

Halliwell, G. R., Jr., and J. S. Allen, CODE-1: Large-scale wind and sea level observations, CODE-1: Moored Array and Large-Scale Data Report, *WHOI Tech. Rep. 82-23*, edited by L. K. Rosenfeld, pp. 139–185, Woods Hole Oceanogr. Inst., Woods Hole, Mass., 1983.

Halliwell, G. R., Jr., and J. S. Allen, Large-scale sea level response to atmospheric forcing along the west coast of North America, summer 1973, *J. Phys. Oceanogr.*, *14*, 864–886, 1984.

Halliwell, G. R., Jr., and J. S. Allen, CODE-2: Large-scale wind and sea level observations, CODE-2: Moored Array and Large-Scale Data Report, *WHOI Tech. Rep. 85-35*, edited by R. Limeburner, pp. 181-234, Woods Hole Oceanogr. Inst., Woods Hole, Mass., 1985.

Halliwell, G. R., Jr., and J. S. Allen, Wave number–frequency domain properties of coastal sea level response to alongshore wind stress along the west coast of North America, 1980–1984, *J. Geophys. Res.*, in press, 1987.

Halliwell, G. R., Jr., H. L. Pittock, V. M. Halliwell, and J. S. Allen, The CODE large-scale meteorological, sea surface temperature, and coastal sea level data set, *Data Rep. 125*, *Ref. 86-15*, Coll. of Oceanogr., Oreg. State Univ., Corvallis, 1986.

Holl, M. M., and B. R. Mendenhall, Fields by information blending, sea level pressure version, 66 pp., Numerical Weather Center, Meteorology International, Inc., Monterey, Calif., 1971. (*Tech. Note 72-2*, 66 pp., Fleet Numerical Weather Central, Monterey, Calif., 1972.)

Hsu, S. A., Models for estimating offshore winds from nearby onshore meteorological measurements, *Boundary Layer Meteorol.*, *20*, 341–351, 1981.

Hsu, S. A., Correction of land-based wind data for offshore applications: A further evaluation, *J. Phys. Oceanogr.*, *16*, 390–394, 1986.

Hsueh, Y., and R. D. Romea, A comparison of observed and geostrophically calculated wintertime surface winds over the East China Sea, *J. Geophys. Res.*, *88*, 9588–9594, 1983.

Kundu, P. K., Ekman veering observed near the ocean bottom, *J. Phys. Oceanogr.*, *6*, 238–242, 1976.

Mass., C. F., M. D. Albright, and D. J. Brees, The onshore surge of marine air into a coastal region of complex terrain, *Mon. Weather Rev.*, in press, 1986.

Mooers, C. N. K., A technique for the cross spectrum analysis of pairs of complex-valued time series, with emphasis on properties of polarized components and rotational invariants, *Deep Sea Res.*, *20*, 1129–1141, 1973.

Neiburger, M., D. S. Johnson, and C. Chien, Studies of the structure of the atmosphere over the eastern Pacific Ocean in summer, I, The inversion over the eastern North Pacific Ocean, *Univ. Calif. Publ. Meteorol.*, *1*, 94 pp., 1961.

Rienecker, M. M., and C. N. K. Mooers, Comparative spectrum analyses of surface wind stress fields based on NDBC winds and FNOC analyses, in *Proceedings of the 1983 Symposium on Buoy Technology*, pp. 281–285, Marine Technology Society, Washington, D. C., 1983.

Thomson, R. E., A comparison between computed and measured oceanic winds near the British Columbia coast, *J. Geophys. Res.*, *88*, 2675–2683, 1983.

Winant, C. D., R. C. Beardsley, and R. E Davis, Moored wind, temperature, and current observations made during Coastal Ocean Dynamics Experiments 1 and 2 over the northern California continental shelf and upper slope, *J Geophys Res.*, this issue.

J. S. Allen, College of Oceanography, Oregon State University, Corvallis, OR 97331.

G. R Halliwell, Jr., Graduate School of Oceanography, University of Rhode Island, Narragansett, RI 02882.

(Received May 1, 1986;
accepted July 7, 1986.)